Universitetet i Stavanger

FACULTY OF SCIENCE AND TECHNOLOGY

MASTER'S THESIS

Study programme/specialisation: Masters (Petroleum, Natural Gas Engineering)	Spring semester,2017 Open
Author: Roshan Ravindra Shetty	…………………………………………… (signature of author)
Programme coordinator: Prof. Dr. Zhixin Yu Supervisor: Prof. Dr. Zhixin Yu	
Title of master's thesis: CO_2 Methanation over Carbon Nanotubes Supported Nickel Catalyst	
Credits:30 ECTS	
Keywords: Nickel Carbon Nanotubes Surface Functionalization Catalysts CO_2 Methanation	Pages: 60 Stavanger, 15/06/2017

ABSTRACT

CO_2 hydrogenation to methane has become one of the most researched area due to the possibility of reducing CO_2 emissions and at the same time to be utilized in the power-to-gas or biogas upgrading technology. Catalyst is the medium through which in terms of kinetic rates and selectivity, the efficient CO_2 conversion is possible. This thesis deals with the development of nickel based catalysts supported on carbon nanotubes to evaluate their potential for CO_2 methanation. Multiwalled carbon nanotubes (CNT) with three different inner-outer diameters (CNT1020, CNT2040 and CNT4060) were used as a support. One of the major focus was the surface functionalization of CNTs with oxygen and nitrogen groups to see the effect of surface doping on the catalyst performance for CO_2 methanation.

Surface functionalization of the CNTs with oxygen was done by refluxing with nitric acid. And nitrogen doping was done by further post treatment with ammonia as nitrogen precursor. Nickel supported on original, oxidized and nitrogen doped CNT catalysts were prepared by incipient wetness impregnation.

Several characterization was performed to evaluate the physical and chemical properties of the catalysts. FTIR, Raman and TGA showed that modification by oxygen doping has successfully introduced Oxygen containing groups, while the Nitrogen doping is less successful. N_2 physisorption study demonstrated obviously that CNTs with smaller diameter had higher surface areas, which further increased upon doping with oxygen. The XRD characterization showed close but small particle sizes for all the CNTs supported catalyst. TPR study also presented that the reduction behavior and reducibility of different catalysts were close. BET showed a slight increase in the impregnated catalysts than the CNTs due to better porous structure developed during calcination. H_2 Chemisorption however, demonstrated that oxygen doped Ni catalyst had high dispersion, while the Nitrogen doped catalyst had the lowest dispersion.

The catalysts were tested for CO_2 methanation at the same condition of 350 ^{o}C, 1 atm with a H_2/CO_2 ratio of 4 in a fixed bed reactor for 16 hr. It was found that the functionalized CNTs supported Ni catalysts had lower CO_2 conversion and CH_4 selectivity compared with the original CNTs supported catalysts, which was explained by lower CO_2 and CH_4 capacity after oxygen and nitrogen treatment. The CNT1020 supported nickel catalyst showed highest conversion of 43% and selectivity of 91% when compared to other CNTs supported Ni catalysts.

Contents

List of Figures

List of Tables

Chapter 1: Background and Literature Review

CO_2 emissions have been increasing from last decades which has served as a main cause of greenhouse effect. This has led to growing environmental concerns in terms of utilization of fossil fuels as energy sources, with effects such as global warming, ocean acidification and weather change [3]. It is expected that more than 40 Gt of CO_2 will be emitted if it is continued in this way by 2030 [4]. European union has set a tight target by 2050 to reduce greenhouse gas emissions by around 60-80% [5]. Therefore a solution needs to be found in order to reduce CO_2 emissions. Among which, CCS (carbon capture and storage) and CO_2 conversion to fuels or chemicals are important to achieve the emission reduction target. CO_2 conversion can lead to not only reducing its emissions but also production of fuels and chemicals too. However when we see in terms of supply and demand in the global market chain, the fuel consumption is two orders of magnitude higher than that of chemicals using CO_2 as a feedstock [6]. Between various ways for fuel production, CO_2 conversion using hydrogen as a high energy material for transformation to hydrocarbons is the most researched area [6, 7]. Among which CO_2 hydrogenation to methane is one of the most advantageous processes [8].

The main component of natural gas is methane [9]. The first person to observe the catalytic CO_2 hydrogenation to methane over nickel catalyst was the French chemist Mr. Paul Sabatier [10]. The Sabatier reaction is as shown below:

$$CO_{2(g)} + 4H_{2(g)} \rightarrow CH_{4(g)} + 2H_2O$$
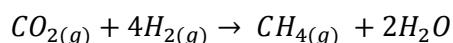
Catalyst is the medium through which the CO_2 conversion to methane in terms of acceptable kinetic rates and selectivity needs to be utilized. The catalysts favorable for methane production are nickel and ruthenium. The less reactive metal constituents like Pd , Ru, Rh and Mo catalyze to different fuels such as methane and methanol simultaneously [11]. Considering high activity and cheap price, nickel compared to ruthenium is commonly studied and will be used in this thesis.

In order for metal to disperse uniformly, a support is required. When it comes to high dispersion, stability and selectivity, support plays an important role [12]. The most common supports used for nickel are silica (SiO_2), Lanthanum (La_2O_3), Alumina (Al_2O_3) and CeO_2-ZrO_2 mixed oxides which are used specifically for CO_2 methanation process [7, 8].

Different from the supports mentioned above, carbon nanotubes (CNTs) have been studied and researched in this thesis. The main reason being its interesting mechanical and electronic properties [13, 14]. The metal supported by carbon nanotubes with high specific surface area in turn gives high dispersion for metal particles [15].The functionalization of the CNTs with oxygen and nitrogen atoms

could potentially improve the properties of CNTs which in turn also influence the catalyst performance in CO_2 methanation .

1.1 Aim and Objective

The main aim is to develop carbon nanotubes supported nickel catalysts which shall in terms of selectivity, stability and activity contribute to an efficient CO_2 conversion to methane process.

The original, oxidized and nitrogen doped CNTs of different external diameters (inner diameter-outer diameter: 10-20, 20-40 and 40-60) were employed as supports of nickel based catalysts. Surface functionalization of CNTs with oxygen and nitrogen doping as well as comparisons with the original ones were done in terms of activity tests for all three types of CNTs. Several characterizations were utilized to study the physical and chemical properties of the catalysts in order to evaluate their influence on the catalyst performance. The type of CNTs used was multiwalled carbon nanotubes.

1.2 Effect of Reaction Conditions on CO₂ Methanation

1.2.1 Thermodynamic Analysis

We firstly analyze the thermodynamics of the reaction in order to evaluate the optimum reaction conditions [16, 17]. The reaction conditions which affect the CO_2 methanation are reaction temperature, pressure, stoichiometric ratio of reactant H_2/CO_2 and also the addition of other reactants such as water, methane, oxygen which will influence CO_2 conversion, CH_4 selectivity and carbon deposition.

Gao et al. compared the thermodynamic equilibrium calculation with the experimental over two commercial methanation catalysts by applying total Gibbs free energy minimization method [2]. Table 1 lists the main and side reactions taking place for conversion of CO_2 to methane.

Table 1: Main and Side Reactions involved in CO₂ Methanation [2].

Reaction Number	Reaction formulae	ΔH(298K) KJ mol^{-1}	Reaction type
R1	$CO + 3H_2 \leftrightarrow CH_4 + H_2O$	-206.1	CO methanation
R2	$CO_2 + 4H_2 \leftrightarrow CH_4 + 2H_2O$	-165.0	CO₂ methanation
R3	$2CO + 2H_2 \leftrightarrow CH_4 + CO_2$	-247.3	Inversed CO2 methane reforming
R4	$2CO \leftrightarrow C + CO_2$	-172.4	Boudouard reaction
R5	$CO + H_2O \leftrightarrow CO_2 + H_2$	-41.2	Water gas shift
R6	$CH_4 \leftrightarrow 2H_2 + C$	74.8	Methane cracking
R7	$CO + H_2 \leftrightarrow C + H_2O$	-131.3	Carbon monoxide reduction
R8	$CO_2 + 2H_2 \leftrightarrow C + 2H_2O$	-90.1	Carbon dioxide reduction

 To analyze the CO_2 methanation with respect to reaction conditions, Van't Hoff equation could be used to calculate the equilibrium constant so that it shall predict the equilibrium value in the typical reaction temperature range [2].
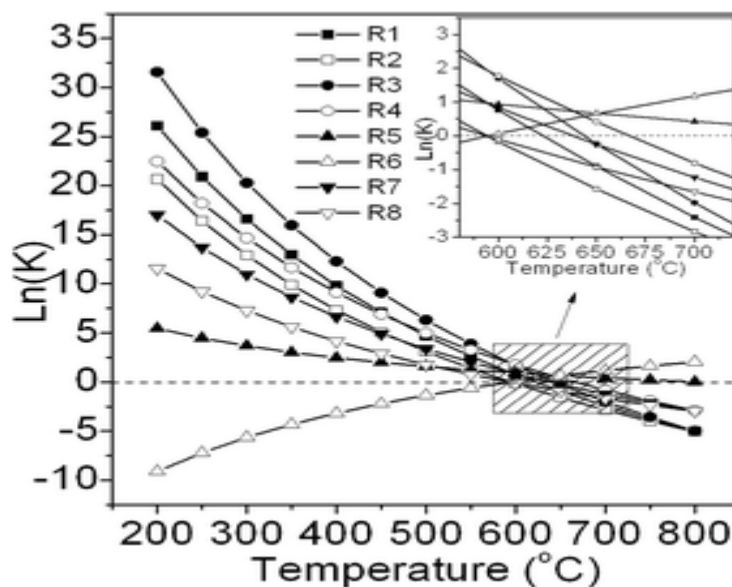
Figure 1. Equilibrium constant calculated as a function of temperature[2]

As shown in Figure 1 above, higher equilibrium constant in the range of 200-500°C made the exothermic CO_2 methanation reaction suppressed as the temperature increased [2].
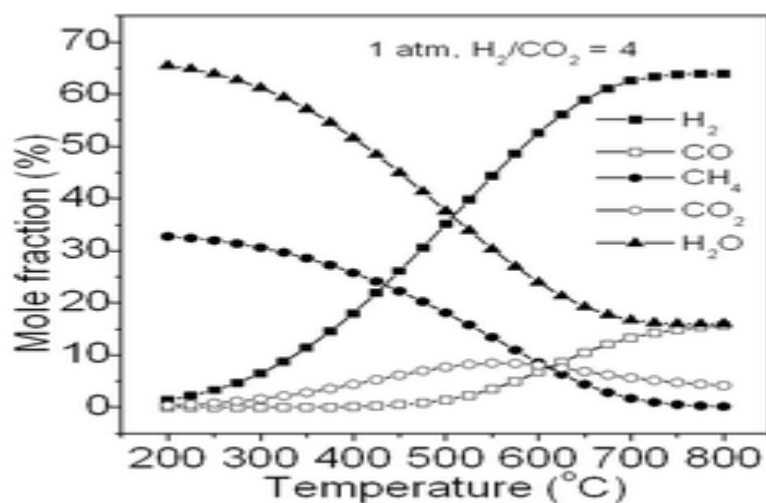
Figure 2: Products formed with respect to change in temperature [2].

In order to investigate the products formed with respect to the temperature, Figure 2 best explained the required temperature for CO_2 methanation process. Gibbs free minimization was used to determine the fraction of products formed at equilibrium keeping stoichiometric ratio H_2/CO_2 to 4:1 at 1 atm pressure. Methane was the main product at temperatures below 450°C. As temperature increased beyond 450°C, carbon monoxide was formed by reverse water gas shift reaction (Table 1). CO_2 methanation thereby was favored at lower temperatures [2, 11].
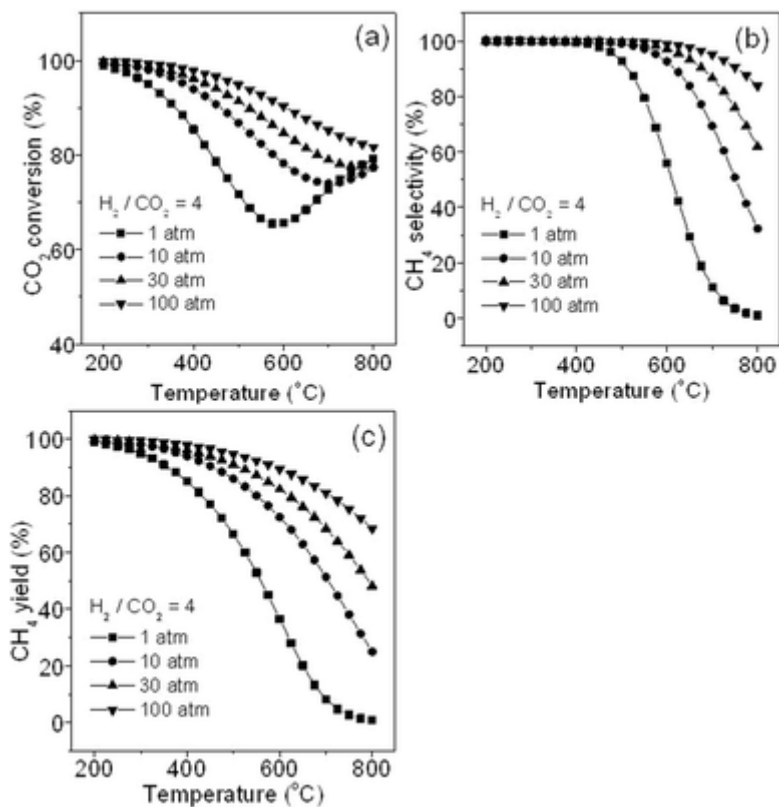
Figure 3: Effect on CO_2 conversion , CH_4 selectivity and CH_4 yield with respect to change in temperature and pressure [2].

From figure 3 the CH_4 yield and selectivity were clearly favored at lower temperatures and high pressures. It was observed that CO_2 conversion decreased when temperature increased until around 600^oC. Beyond this temperature the reverse water gas shift reaction came as a main reaction consuming CO_2, which as a consequence increased the conversion of CO_2, while the CH_4 yield and selectivity decreased [2, 11].
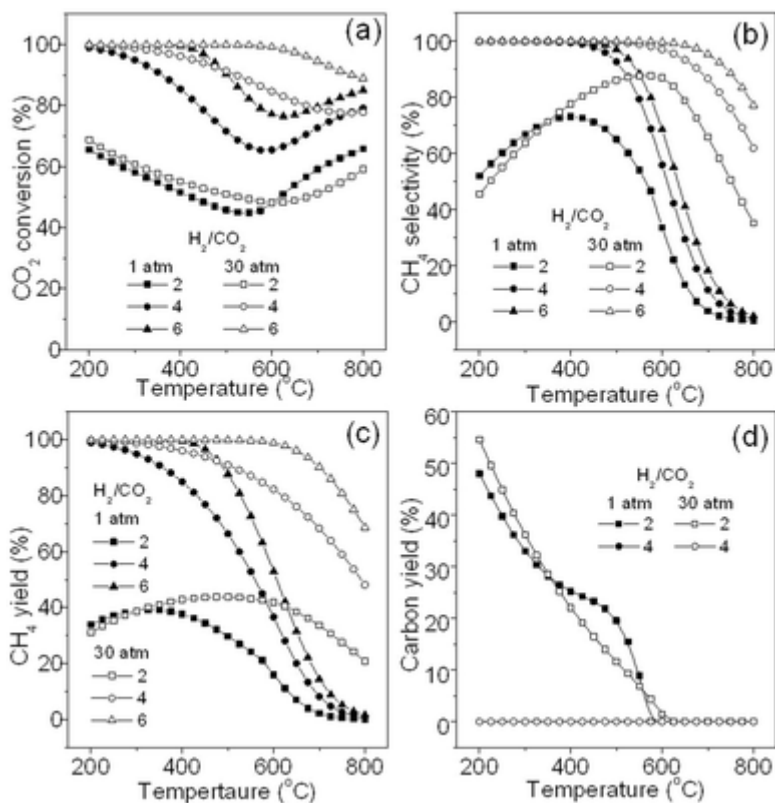
Figure 4: Effect on methanation reaction with respect to change in stoichiometric H_2/CO_2 ratio [2].

As it is clear from Figure 4 that with an increase in ratio of H_2 molecules with respect to CO_2, the methanation reaction was favored. So increase in stoichiometric ratio of the reactants H_2/CO_2 clearly influenced the reaction products [18].

The Gibbs free minimization method approach therefore showed that lower temperature, higher pressure and stoichiometric ratio of 4 or above favored the methanation reaction [2].

1.2.2 Effect of Gas hourly space velocity (GHSV)

Gas hourly space velocity is defined as the following:

$$GHSV = \frac{Volumetric\ Flow\ rate\ of\ the\ reactants\ at\ STP(H2\ and\ CO2)}{Total\ Catalsyt\ volume}$$

STP = Standard Conditions

From the above equation it is clear that there is an inverse relationship between GHSV and the conversion of the reactants. It tells that if GHSV is higher, the amount of time spent by the reactants

on the catalyst and in the reactor is shorter, which subsequently decreases conversion of CO_2 to methane.

Abate et al. [19] studied the effect of GHSV at different temperatures on CO_2 methanation on a Ni/Al_2O_3-TiO_2-CeO_2-ZrO_2 catalyst between 250-400°C . They found that the CO_2 conversion were higher below 350 °C. When the operation was carried out below thermodynamic equilibrium, the higher GHSV resulted in a decrease of the CO_2 conversion.

1.2.3 Effect of Initial CH$_4$ concentration in feed

If we consider taking biogas (by definition a mixture of CO2 and CH4) directly for conversion to methane without extracting CO_2, the presence of CH_4 shall affect the CO_2 conversion. The effect is mainly carbon deposition occurring at temperature above 400°C due to methane cracking reaction, which will influence the catalyst activity [2]. According to Le Chatelier's principle, the presence of CH_4 move the equilibrium to the left, further influence the conversion of CO2. Jurgensen et al. [20] investigated the effect of CH_4 on CO_2 conversion by thermodynamic calculations. It was shown that at 1 bar when the concentration of CH_4 was about 60%, the CO_2 conversion decreased from 96% to 92%. But when the pressure is increased above 8 bars, the effect on conversion is not big. Therefore it is not necessary to remove CH_4 from the feed gas if Sabatier reaction is carried out at elevated pressures.

1.2.4 Effect of Contaminants in feed

The flue gases which are emitted from the conventional power plants are also been used as feed for methanation. This mainly consist of CO_2, N_2, O_2, H_2O and some contaminants like SO_2 and NO_2 [21]. NO_2 doesn't have much effect on the performance of the CO_2 conversion to methane. However, SO_2 has a significant effect on the catalytic performance as shown in Figure 5.
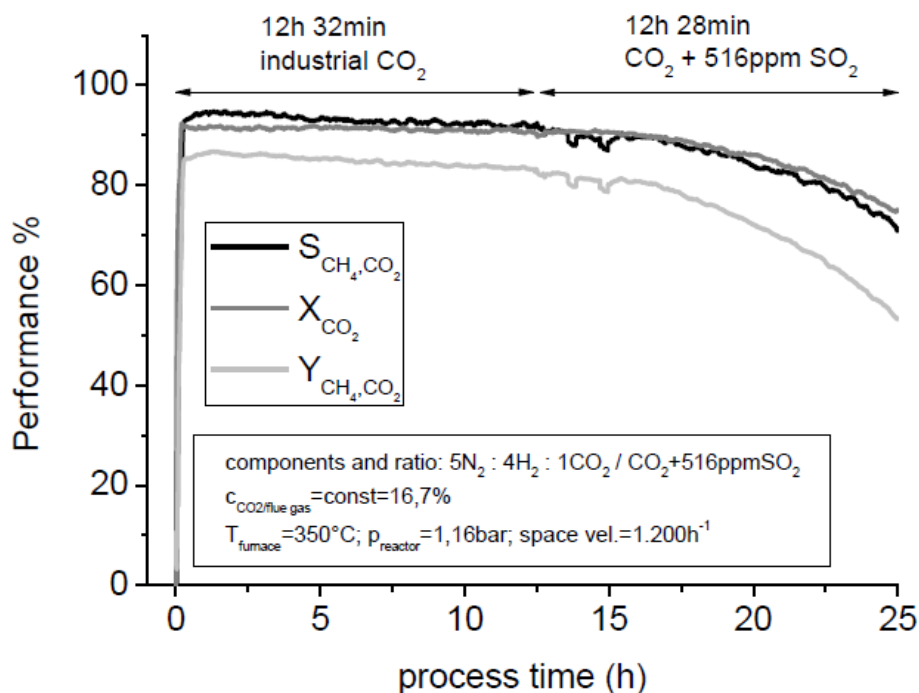
Figure 5: Effect of SO₂ on catalytic performance [21].

It can be observed that for the first 12.5 hours with only CO_2 in the feed stream, the performance of the catalyst is stable. After that when SO_2 is added to the feed, a decrease in the catalytic performance by 17% is observed. This degradation is caused mainly due to formation of strong bond between the sulphur and metal catalytic sites [22].

The possible way to prevent this would be to regenerate the sulphur poisoned catalyst by treatment with steam or steam-air mixture [21, 23]. Another way would be to use active coal for SO_2 adsorption for an efficient removal of sulphur [21].

1.2.5 Effect of water vapor on CO₂ methanation

A considerable amount of water could be formed in the process of CO_2 methanation (Table 1). The presence of water have a negative effect on the rate of methanation.

Over nickel supported on mesoporous silica nanoparticles catalysts, it has shown that (figure 6) a decrease in activity by about 30% in presence of water vapor. This negative effect was mainly due to water gas shift reaction, which formed CO_2 as a product. Since the support was hydrophilic, the adsorption of water caused the hydrolysis of Si-O-Si bond, which thereby resulted in damage of the

structure of the support [24, 25]. Furthermore, the presence of water vapor also increased the rate of sintering of Ni metal species [26].
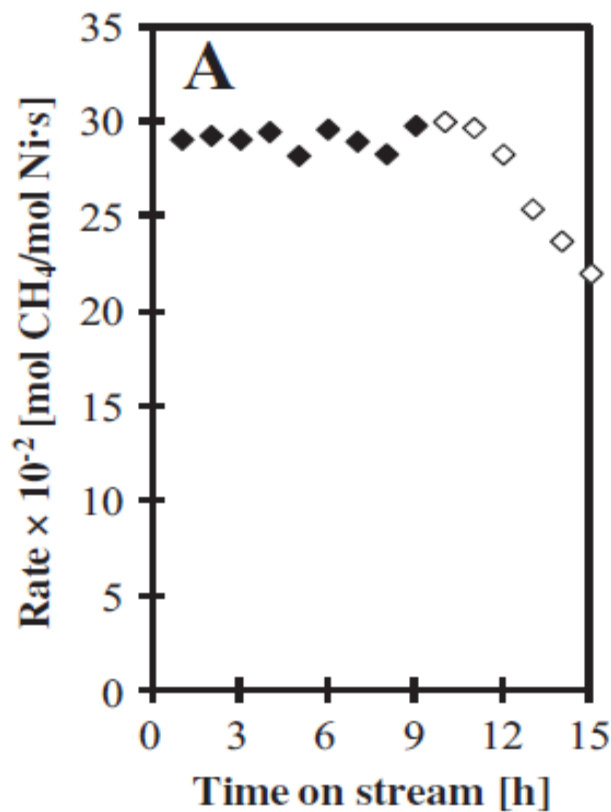
Figure 6:Effect of water vapor on methanation reaction [24]: the black square indicating absence of water vapor; white square indicating presence of water vapor.

1.3 Methanation Catalysts

1.3.1 Support

The interaction between metal and support is very important for the performance of a catalyst. It in fact has a big influence on the stability, active site dispersion and activity. The supports used in this thesis were carbon nanotubes of multiwalled nanotubes type with 3 different internal and external diameters (CNT-1020, CNT-2040, and CNT-4060).

Carbon nanotubes

Carbon nanotubes were chosen mainly because of their interesting electronic and mechanical properties, stability, surface functionality, etc [27]. Due to its unique morphology and structure, it possesses unique properties as catalyst supports when compared to metal oxide supports. Since this type of carbon sample is in nano scale, it could exhibit higher surface area. Due to the higher surface area, the dispersion of the metal species is high and this influences the catalytic activity in terms of higher amount of surface active sites available for the methanation reaction.

Types of carbon nanotubes

CNTs are the set of carbon atoms arranged in the form of hexagon structure which are been rolled into tubes and are also known as rolled up graphene sheets.

The carbon nanotubes are classified based on the number of graphene sheets they have in their structures [28]: 1) Single walled carbon nanotubes 2) Multi walled carbon nanotubes

Single wall Nanotubes

One atom thick layer of graphene rolled into a cylinder conceptualizes the structure of single walled carbon nanotubes. The pair of indices (m, n) called chiral vector gives an idea of how the graphene sheet is rolled. The direction in which the graphene sheets rolled are denoted by these indices. The structure is zigzag if m=0 which attributes to the hexagonal pattern when moved on the tubes circumference. The structure is armchair if m=n. And the structure is chiral if the value of m is between zigzag and armchair which indicates the capability of the tubes to roll in either directions [29, 30].
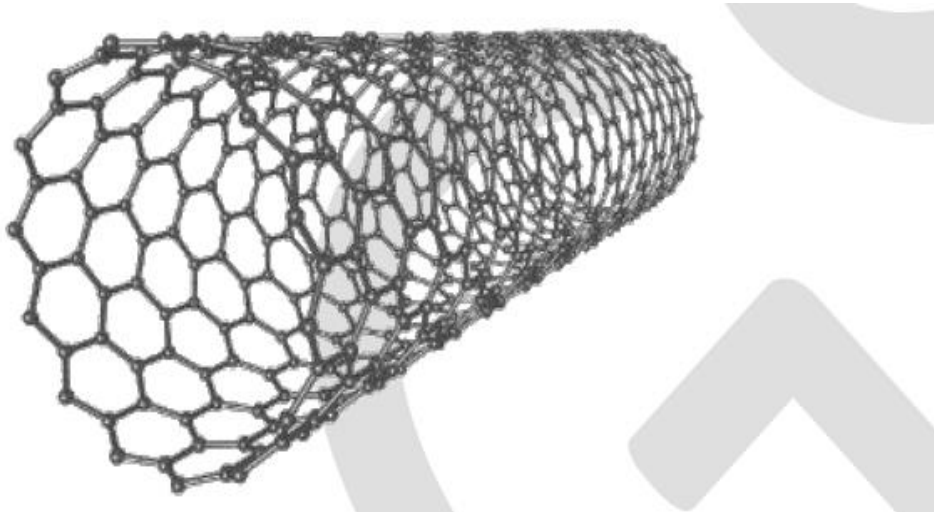
Figure 7: Structure of Single wall nanotubes (SWNT) [28].

Multiwalled Carbon Nanotubes

Multiwalled carbon nanotubes are the set of concentric rings of single walled nanotubes (Figure 8) arranged in the form of a continuous increasing radii. Similar to the inter graphene distance, the spacing between the concentric walls are 0.34 nm. Depending on the tubes having common axis, the multiwalled carbon nanotubes have outer diameter in the range of 2-100 nm. They are structurally mesoporous and the surface area depends on the number of walls. The length varies from few to hundreds µm [31].
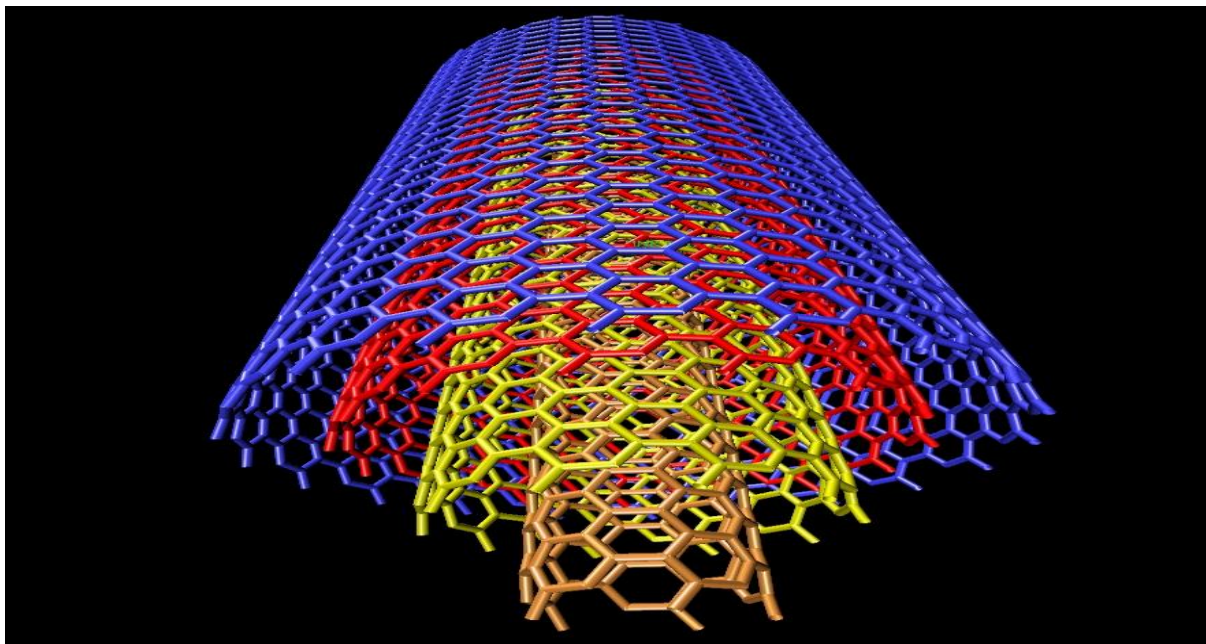
Figure 8: Structure of Multiple Walled Nanotubes [28].

Surface Functionalization of the Carbon Nanotubes

In order to improve the surface area, metal-support interaction, purity and CO_2 adsorption capacity, it is important to introduce functional groups like oxygen or nitrogen onto the surface of the support which can have influential effect on the activity of the catalysts. The influence of two functional groups is discussed and experimentally done in this thesis.

Oxygen Doping of Carbon Nanotubes

Carbon nanotubes have impurities and residual metal catalyst on the surface. So before impregnating metal species, it is important to reflux or oxidize the samples with nitric acid (HNO_3). Introducing oxygen functional groups gives a better bonding between the metal species and support. Acid refluxing removes the amorphous carbon impurities, residual metal catalysts and opens the pores, resulting in increase in surface area of the carbon samples. Also the opening of the tube ends of CNTs on refluxing with acid has an influence on the increase in specific surface area.

Nitrogen Doping of Oxidized Carbon Nanotubes

In order to modify the electronic structure of the carbon supports, doping of carbon nanotubes with heteroatoms is a practical way to adjust both physical and chemical property [27, 32-34] . Due to the similarity in the atomic size when compared to the carbon atom, nitrogen happens to be one of the most effective dopant. Due to which there is easy accessibility for entering the nanotube lattice [35, 36]. Nitrogen doping may result in significant changes in physical, chemical and electronic structure of CNT, and has received a lot of attention by researchers. The electronic properties of the carbon samples are enhanced by additional pair of electrons on N atoms when doped with respect to the π system of graphite like hexagonal framework structure of carbon [37-39]. Due to a narrow energy gap, the N doped CNTs have increased CO_2 storage capacity [37, 40]. During the doping, the nitrogen atoms as substituents of carbon enter the graphene sheets altering the adsorption capacity of the nanotubes. This modification for application in catalysis shall theoretically improve the catalytic activity as well as the selectivity of the catalysts [41].

Figure 9 below shows the structural representation of the presence of oxygen and nitrogen atoms after doping on CNTs.
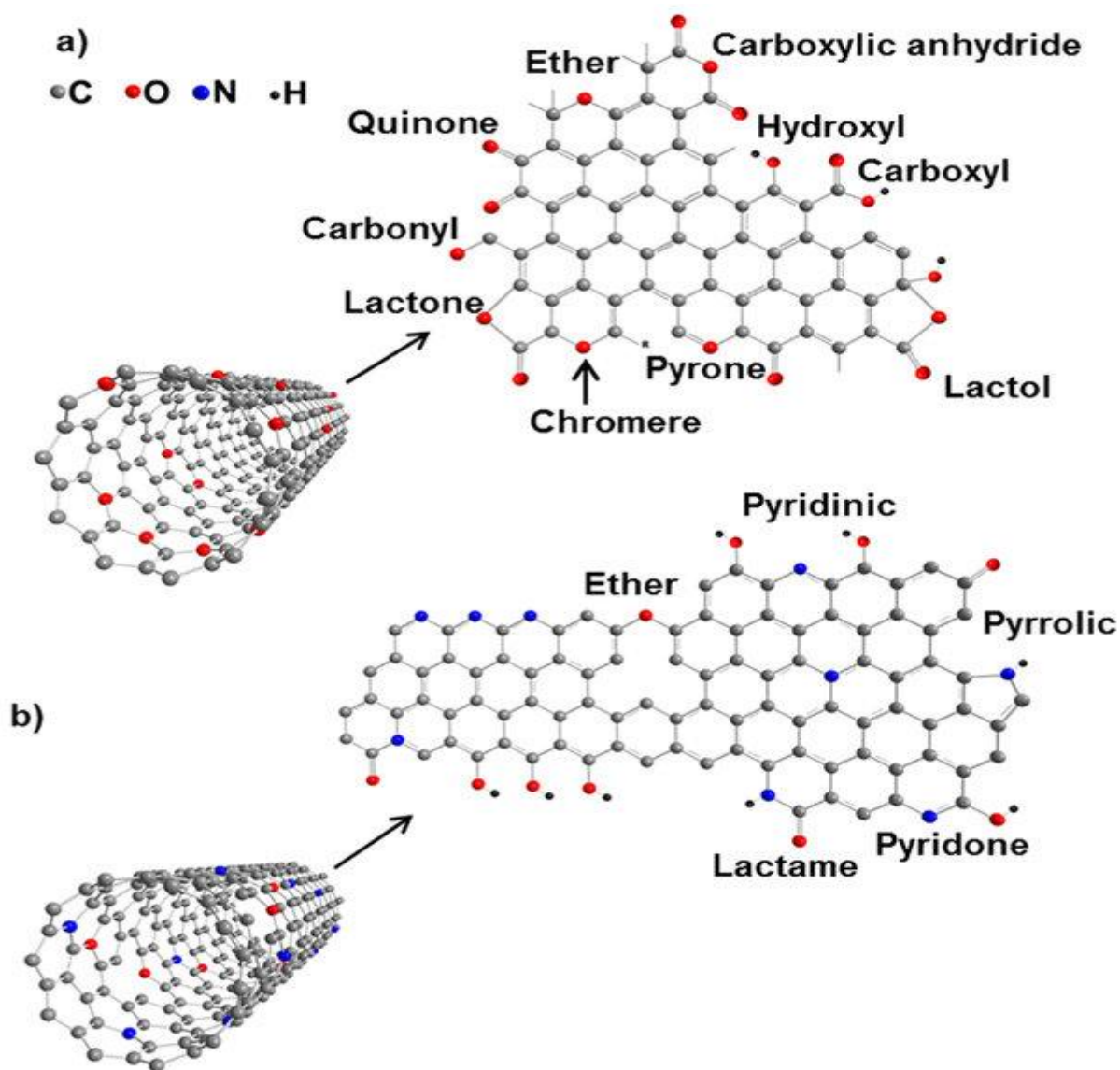
Figure 9: Structural representation of CNTs; a) oxygen doped, b) nitrogen doped. [42]

1.3.2 Metal species

Generally metal species for catalysis are made from group VIII, IX, X, XI transition elements [11]. Metals which are highly selective to methane are nickel and ruthenium. In this thesis nickel is been chosen as the metal species mainly due to its high activity and relatively low price [11]. Ruthenium has excellent activity but it is a very expensive precious metal [43].

For catalyst preparation, one of the factor to consider is the metal loading. The metal loading on a support shall affect pore size, pore volume, and dispersion. A reduced surface area is mainly caused due to the agglomeration of metal species leading to the blockage of the porous structure [11]. The

active sites available for reaction might increase with the loading of metal but the dispersion normally decreases [44].

1.3.3 Catalyst Deactivation

The catalyst performance in terms of activity will after some point decreases eventually [31].

There are 3 main catalyst deactivation mechanisms [31]: 1. Fouling; 2. Poisoning; 3. Sintering.

Fouling

When there is a deposition of a substance on the active metal sites of the catalyst, deactivation occurs. The substance which mainly contribute to this is carbon. Carbon occupies the metal active sites and also block the pore structures of a catalyst leading to fouling. Since this type of deactivation mechanism is reversible, regeneration can be done by heating in presence of air to remove fouling [31].

Poisoning

The chemical bonds formed between the impurities in feed and the active metal sites of the catalysts contribute to the poisoning. Impurities like sulphur are usually chemisorbed on metals like nickel, which can be either reversible or irreversible [31]. If the bond is weak, then the catalyst can be regenerated by removing the poison in the feed. If the bond is strong, then regeneration is complicated [31].

Sintering

Higher temperature causes a negative effect on the specific surface area of the catalyst and thereby modifies the structure and also change chemical properties of catalyst resulting in reduced activity [31]. This is independent of fluid composition entering the reactor when compared to fouling and poisoning. That's the reason why it's also termed independent deactivation [31]. In order to prevent this, the focus should be on to design reactors in such a way that there is little potential for thermal deactivation.

1.4 Reaction Mechanism of CO_2 Methanation

In order to understand the process or the route of reaction towards the formation of methane from carbon dioxide, it is important to understand the reaction intermediates formed in between the process [11]. As these intermediates formed can play a role in CO_2 methanation. There are mainly two types of mechanisms involved: 1) Formation of carbon monoxide (CO) as an intermediate [45-49], 2) Direct conversion of CO_2 to methane without CO as intermediate[50, 51].

Figure 10 shows a brief schematic representation of the reaction pathways of CO_2 methanation.
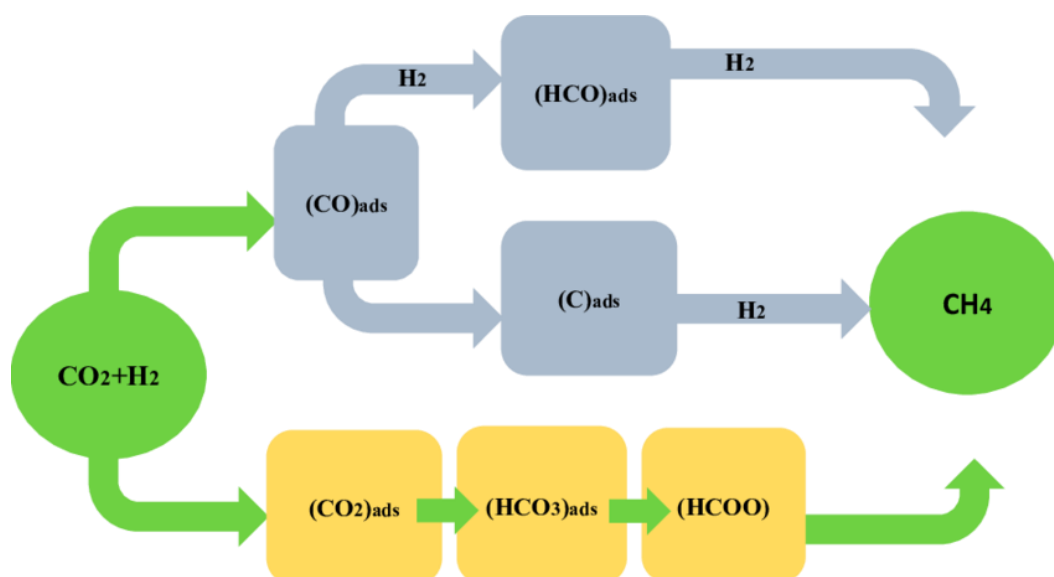
Figure 10: Possible reaction routes of CO_2 methanation [1].

1.4.1 Formation of CO (Carbon Monoxide) as an intermediate

In this mechanism, firstly CO_2 is reduced to CO and then CO converts to methane. The main point to observe here is that the reduction to CO is unfavorable at reaction temperatures of 200-400°C. In order to prevent this, we could control the process by kinetics. CO methanation should be proceeded faster than its reduction from CO_2 such that there would be no CO in the exit stream of a reactor. The following reactions shows the reaction pathways for CO_2 to methane with CO as an intermediate.

$$CO_2 + H_2 \leftrightarrow CO + H_2O$$

$$CO + 3H_2 \leftrightarrow CH_4 + H_2O$$
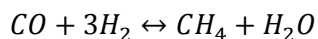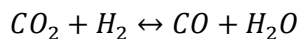
Whereas alternative way for having CO as an intermediate was suggested by Wagner et al. [52], who showed that carbon dioxide first dissociated into carbon monoxide and oxygen which were in the adsorbed state.

$$CO_{2(ads)} \rightarrow CO_{(ads)} + O_{(ads)}$$
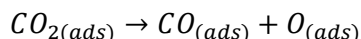
Then the adsorbed carbon monoxide was transformed to methane, and water formed from adsorbed oxygen reacted with molecular hydrogen which was a rate determining step.

$$H_{2(g)} + O_{(ads)} \rightarrow H_2O_{(ads)}$$

$$CO_{(ads)} \rightarrow CH_4$$
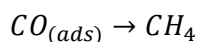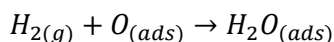
As an example, CO_2 methanation over a Ru/TiO_2 catalyst with 5 wt. % metal loading progresses via formation of adsorbed CO as an intermediate, which comes mainly from the reverse water gas shift reaction. The (TiO_2)Ru-CO complex formed at the metal support interface forms a partially oxidized carbonyl species, on reacting with adsorbed hydrogen atoms it produces methane in the gas phase [53].

1.4.2 Direct conversion of CO₂ to methane without CO as intermediate

In this mechanism, the CO_2 conversion to methane doesn't have CO as an intermediate in the reaction pathway. The adsorbed CO_2 produces formates and carbonates and then react with hydrogen to form methane as shown in Figure 5.

CO_2 is negatively charged at low temperatures and is chemically bonded through carbon atom [54]. When CO_2 is fed to the reactor over a catalyst, an electronic charge is taken from metal which result in binding on the surface. When hydrogen molecule reacts with the adsorbed CO_2, a H-CO_2 bond is formed on the surface via two oxygen atoms and hydrogen atoms bonded with the carbon atom, giving formate as an intermediate product in the reaction [11, 54]. The reason for no formation of CO is due to the presence of hydrogen [54].

For example, on a $Ce_{0.95}Ru_{0.05}O_2$ catalyst, there is no formation of CO as the reaction intermediate in the process of CO_2 methanation [55]. When temperature programmed reaction experiment is carried out on the catalyst, CO hydrogenating doesn't show any activity at all for CO conversion to methane.

Another example would be the nonporous gallium oxide which is also a catalyst for direct hydrogenation of CO_2 to methane [56].

Chapter 2: Experimental

2.1 Catalyst preparation

There are lot of methods to impregnate metal precursor on the support. In this thesis incipient wetness impregnation was used for impregnating nickel precursor salt (nickel nitrate hexahydrate) on carbon nanotubes support.

2.1.1 Incipient Wetness Impregnation

Incipient wetness is used to prepare all catalysts. A metal is impregnated on the support by dropwise addition of the metal precursor solution by stirring until the volume adsorbed by the solid support surface is equivalent to the pore volume of the support.

Before impregnation, it is important to know the amount of water to be used for preparing metal precursor salt solution. In the preparation, the pore volume of the support is firstly determined by water. Distilled water is added dropwise while stirring the support until the volume of the water added is equal to the pore volume of the support. This can be observed by the appearance of the support when it changes into being slightly sticky which shows a glistening appearance.

Next the metal precursor solution is prepared by dropwise addition of the solution onto the support. The impregnated samples are dried at 120°C overnight.

2.1.2 Incipient Wetness Calculation

Pore volume of support:

Weight of the support to be weighed (g) = X

Amount of water added (ml) = Y

Pore volume (ml/g) = $\dfrac{Amount\ of\ Water\ Added\ (ml)}{Weight\ of\ the\ support\ (g)}$

For catalyst preparation:

Weight of the dried support (g) = Z

Amount of water to be added (ml): Weight of the dried support (g) × Pore volume (ml/g)

To calculate nickel weight fraction:

Ni (Weight fraction %) = $\dfrac{Nickel}{Support+Nickel}$ = a=12%

Amount of nickel in the support:

Amount of nickel (g) = $\dfrac{a \times Support(g)}{1-a}$

Calculate the metal precursor amount required:

Amount Precursor (g) = $\dfrac{Mw(Metal\ Precursor)}{Mw(Metal)} \times Amount\ of\ nickel\ (g)$

2.1.3 Refluxing of CNTs

Refluxing and oxidizing of carbon samples in order to purify, increase the surface area and enhance the metal–support interaction was done, as explained previously. The CNTs with different diameters were oxidized by boiling with concentrated nitric acid. Refluxing with acid was done for 1 hr. at boiling point of concentrated nitric acid at around 120°C. The samples were filtered and washed with distilled water, and dried overnight at 110°C in the oven. Reaction conditions and type of CNTs used for refluxing were defined (Table 2).

Table 2: Type and Reaction Conditions of CNTs used for Refluxing.

Sample name	Temperature (Boiling) (^{o}C.)	Treatment Time (hrs.)
CNT1020	120	1
CNT2040	120	1
CNT4060	120	1

2.1.4 Nitrogen Doping of CNTs

Nitrogen doping of CNTs were done in order to evaluate specially their possible adsorption of CO_2, which might influence its conversion. Some amount of oxidized CNTs were subjected to the nitrogen doping by post treatment method with ammonia as a precursor for nitrogen [57]. They were loaded into a quartz boat placed in the middle of a horizontal quartz reactor [57]. The carbon samples were exposed to the flowing ammonia at 600°C, flow rate of ca. 80 ml/min and treatment time of about 6 hr. Reaction conditions and type of CNTs used for nitrogen doping were defined in Table 3.

Table 3: Type and Reaction Conditions of Oxidized CNTs used for Nitrogen Doping.

Sample Name	Temperature (°C.)	Treatment Time (hrs.)	Flow Rate(ml/min)
OCNT1020	600	6	80
OCNT2040	600	6	80
OCNT4060	600	6	80

2.1.5 Impregnation of Nickel Precursor on CNTs

Before impregnating the nickel precursor-nickel nitrate hexahydrate solution into the carbon samples, it was important to determine the pore volume. The weighed dried carbon samples were used for calculating the required amount of nickel precursor for 12 wt. % nickel loading. Then the prepared nickel precursor solution was added dropwise to the dried carbon support which was simultaneously stirred. The impregnated samples were dried in oven overnight at 120°C. The following preparation conditions for each sample were defined as in Table 4.

Table 4: Preparation conditions of the catalysts.

Metal Precursor/CNT samples	Nickel Loading (%)
Ni/CNT1020	12
Ni/OCNT1020	12
Ni/NCNT1020	12
Ni/CNT2040	12
Ni/OCNT2040	12
Ni/NCNT2040	12
Ni/CNT4060	12
Ni/OCNT4060	12
Ni/NCNT4060	12

2.1.6 Calcination

Calcination converts a metal precursor to its oxide by thermal pretreatment in the presence of air or nitrogen, depending on the type of support used. The calcination gas used here is nitrogen as the carbon support will possibly react with oxygen. The prepared nickel precursor supported carbon samples were transferred to a quartz tube reactor, and the calcination was done in the presence of nitrogen at a flow of 100 ml/min. The temperature was raised to the calcination temperature of 400°C with a ramp up rate of 5 °C/min. The calcination was done for 5 hrs.

Figure 11 presents the schematic drawing of the calcination setup.
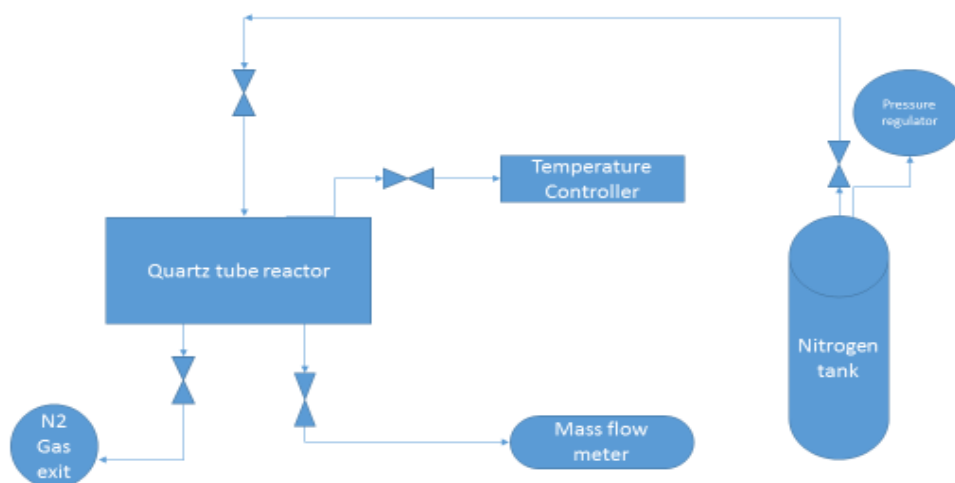
Figure 11: Schematic of the Calcination Setup.

2.2 Catalyst Characterization

2.2.1 Fourier Transform Infrared Spectroscopy

As surface functionalization of oxygen and nitrogen doping on CNTs is done, it is important to analyze the functional groups on the surface. FTIR is well suited to identify the surface functional groups [58].

The surface functional groups are identified in terms of presence or absence of the absorbance with specific wavelengths.

Figure 12 shows the schematic diagram of a FTIR instrument.
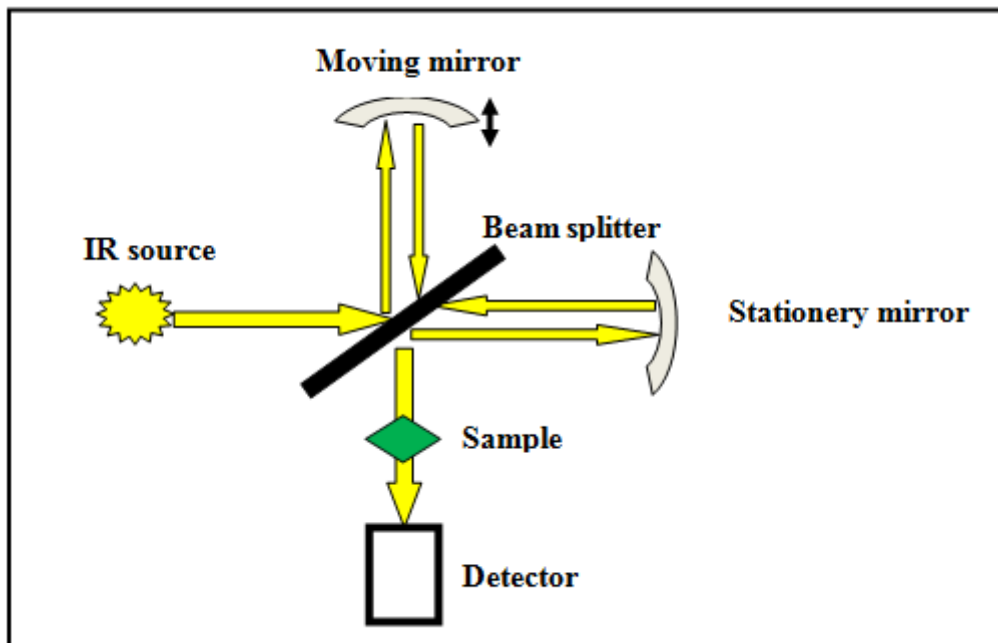
Figure 12: Schematic of the FTIR instrument. [31]

In the analysis, the IR source emitting energy is split into two paths by the beam splitter. Half of them passes through to the stationery mirror and the other half reflects to the moving mirror which moves back and forth at constant velocity indicated by an arrow in the figure above [31].Then the reflected beams recombine at the beam splitter, and there is a difference in the distance travelled by the beam from the moving mirror and the fixed mirror [31].

The recombined beam passes through the sample being analyzed, where some light energy is been absorbed and some transmits to the detector. The energy received is been converted to a spectrum by Fourier transform using algorithm by a software [31]. The information is been transferred from the frequency (ω) domain to a function in time (t) domain by Fourier transform algorithm. The equation to calculate the respective parameters is shown as [31]

$$F(\omega) = \frac{1}{\sqrt{2\pi}} \int_{-\infty}^{\infty} f(t) e^{i\omega t} dt$$

For reference a single beam without a sample is also collected.

The recording of the spectra was done by Nicolet Nexus 670 spectrometer using a deuterated triglycerine sulphate detector [59]. The range of spectra were recorded between 400 and 4000 cm^{-1}

with a resolution of 4 cm^{-1} for 32 scans. For reference, the spectrum of air were used as a single beam radiation [59].

2.2.2 Raman Spectroscopy

Raman spectroscopy gives the molecular structural information of the CNTs on functionalization with oxygen and nitrogen groups. The electronic structures and the vibrational properties of the CNTs are investigated [60]. The rolling of tubes and diameter of the CNTs can also be identified by Raman spectroscopy. The spectra band is specified in terms of D line and G line. The analysis of intensity with respect to the wavelength in Raman determines the quality of the sample. In CNTs the D band represents the existence of defects in the tubes and amorphous carbon, whereas the G band represents the crystallinity of the tubes [42]. The defects in tubes are represented by the high intensity ratio of D band to the G band with respect to the Raman wavelength [42].

Figure 13 shows the schematic flow chart of the Raman spectroscopy instrument.
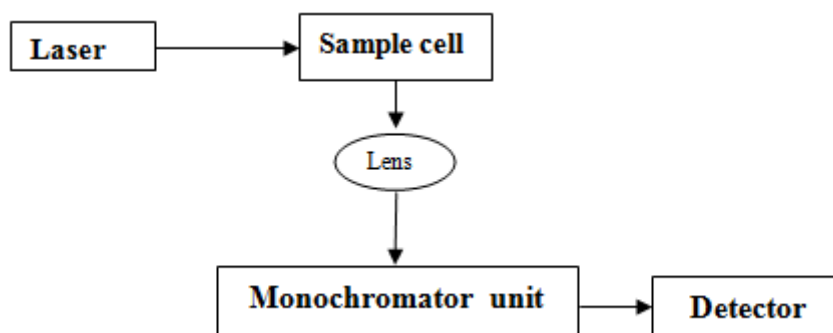
Figure 13: Flow Diagram of the Characterization using Raman Spectroscopy[31].

The samples are placed in a cell or a chamber, and the lights from the laser are been focused on it [31]. As a consequence the lights scattered from the chamber are directed to the entrance of the monochromatic unit. The width of the monochromatic slit is adjusted in such a way that it rejects the undesired spectral resolution and acts as a dispersing unit for the intended radiation to pass through [31]. Then the optical signal passed through the exit is collected and converted to an electrical signal in the detector. The signal is then developed into a final spectrum by processing to a computer [31].

JOBIN YVON HR800 laser confocal Raman spectrometer was used to measure the spectra [59]. These were equipped with a charge coupled device (CCD) camera, an argon ion laser source and an optical microscope [59]. The line in the exit was provided with 50MW power at λ= 514.5 nm by the laser [59]. In order to calculate the band intensities I_D and I_G , the Raman spectra were provided with the facility of Gaussian function to evaluate the band areas[59].

2.2.3 Thermogravimetric Analysis

TGA determines the stability of the material and weight loss with respect to change in temperature. Both in the inert and oxidizing atmosphere the thermal stability of the material can be determined [31].

One of the main catalyst deactivation mechanism by coke deposition also can be quantified by TGA [31].
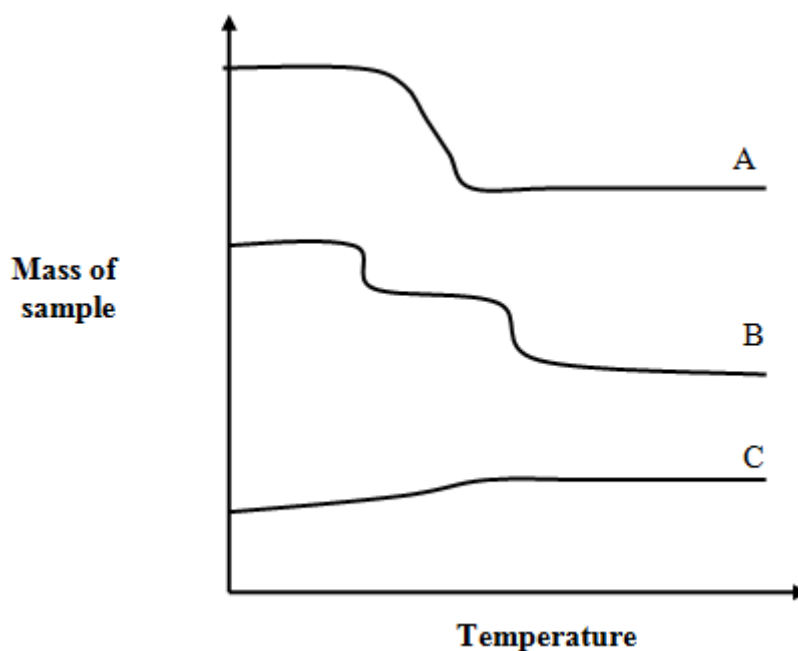
Figure 14: Weight changes with respect to the temperature by TGA[31]

Figure 14 presents three examples of different trends observed with different type of materials showing the change in mass with respect to the temperature change.

Curve A shows the change of mass in a single step. This can be attributed to the removal of moisture, oxidation or the reduction taking place on the material [31].This type of curve can be expected for CNTs subjected to TGA analysis, where after a certain temperature carbon in the presence of air oxidizes to CO and CO_2 [31].

Curve B shows the multiple steps involved in the change of mass. Whereas in Curve C, it is the other way round where there is an increase in mass. This is mainly correlated with the oxidation of the metal in the catalysts [31].

Figure 15 shows the schematic of a TGA instrument.
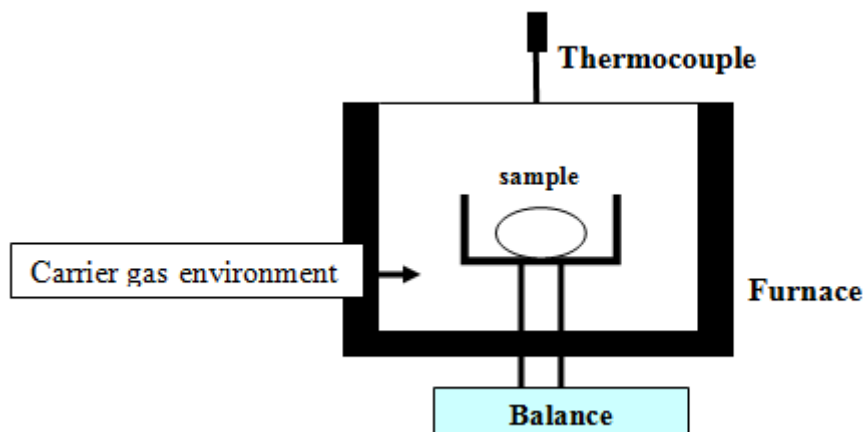
Figure 15: Schematic of a TGA[31].

In this analysis, the samples are placed on a holder and the temperature is increased in a flow of air or inert gas like N_2 or Argon. The weight loss with change in temperature is recorded and plotted [31]. The rate of heating, sample amount, flow conditions of the carrier gas and nature of the carrier gas are factors which affect the TGA analysis [31].

The TGA instrument used was PerkinElmer Pyris 1 [59]. The analysis of the samples were conducted at a heating rate of 10 °C/min from room temperature to 950 °C under air atmosphere with a flow of 50 mL/min [59].

2.2.4 N_2 Physisorption

N2 physisorption measures physical adsorption of gas molecules on the surface of the catalyst with respect to change in relative pressures in order to evaluate specific surface area and pore volume of the catalyst. This is an extension to the Langmuir model which was applied only to monomolecular layer coverage. N_2 physisorption is applied to both mono and multilayers coverage.

The BET equation is correlated between the amount of gas adsorbed with change in relative pressure to monomolecular coverage and is given by the Equation below [61].

$$\frac{1}{[Va(\frac{Po}{P}-1)]} = \frac{C-1}{VmC} \times \frac{P}{Po} + \frac{1}{VmC}$$

Where P= Equilibrium pressure, Po = Saturation Pressure, V_m = Monolayer coverage, V_a= Volume of gas adsorbed at standard conditions, C= constant which is related to enthalpy of gas adsorbed on the catalyst sample.

The pore size distribution are classified based on the diameter of the pores:

Table 5:Pore size Classification [62].

Pore Classification	Width(nm)
Micropores	<2
Mesopores	2-50
Macropores	>50

The mechanism of N_2 physiosorption can be explained in terms of the adsorption isotherm of the mesoporous materials.

Types of Isotherms

Type IV

Closure at P/Po~0.4 indicates presence of small mesopores (hysteresis would stay open longer but for the tensile-strength-failure of the nitrogen meniscus.

Rounded knee indicates approximate location of monolayer formation.

Hysteresis indicates capillary condensation in meso and macropores.

Low slope region in middle of isotherm indicates first few multilayers

Volume adsorbed

Relative Pressure (P/Po)

© 2004-2006 Quantachrome Instruments

Figure 16: Adsorption Isotherm of mesoporous material [63].

The plot explains the mechanism of evaluation of the BET surface area and BJH pore size distribution on how nitrogen interacts with the material. When nitrogen is introduced onto the samples, in the initial stage the surface begins to adsorb the gas molecules forming a monolayer coverage. This allows to evaluate the specific surface area at low relative pressure as shown in Figure 16. Further increase in pressure causes the gases to adsorb over the initially adsorbed gas forming a multilayer coverage. Condensation of the above formed gases over monolayer coverage will occur, filling up the smaller

pores first and then the larger pores. When a saturation pressure is reached, all the pores are completely filled with the condensed N_2 gas, which allows to evaluate pore size, pore diameter and pore volume. As the pressure is reduced the condensed gas is vaporized, this results in emptying of pores and the surface follows a hysteresis loop with a desorption isotherm.

Figure 17 shows the basic schematic of the N_2 physisorption instrument.
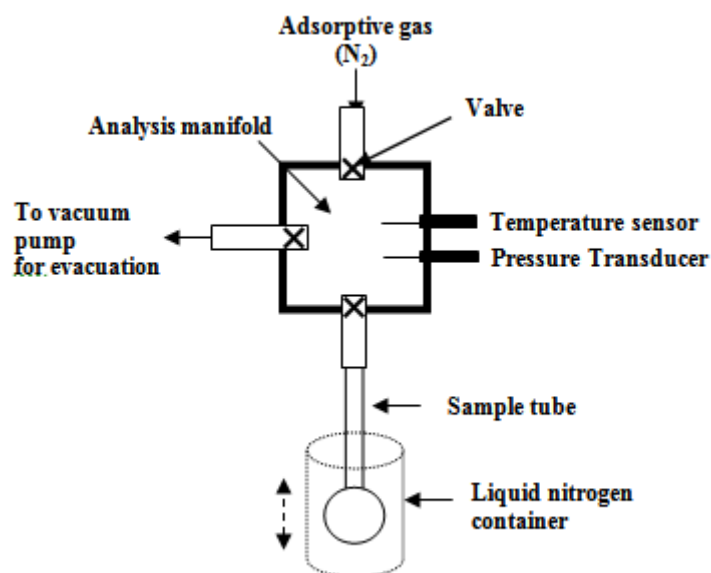
Figure 17: Basic Schematic of the N_2 adsorption-desorption[31].

The experiment starts with the evacuation of the samples at 120-250°C. Then it is subjected to cooling at cryogenic temperature of 77 K by liquid nitrogen [31]. The partial pressure of the nitrogen is slowly increased from 0.1 to 1. As this progresses some amount of gas is adsorbed on the samples. Then the equilibrated pressure is recorded together with the adsorbed amount of N_2 at each point. The measurement will give an isotherm plot of volume adsorbed with respect to the relative pressure. When the relative pressure reaches the saturation point, a complete adsorption isotherm is developed like the one shown in Figure 17. The pressure of the N_2 gas is increased stepwise over the sample [31]. The stepwise reduction in pressure is followed to give desorption isotherm until a low pressure over the sample is achieved [31].

Micromeritics ASAP 2000 surface analyzer was used to measure the N_2 adsorption-desorption at cryogenic temperature of 77 K. In order to remove the moisture on the samples to be tested before analyses, degassing was carried out in vacuum at 120 °C overnight.

2.2.5 X-ray Diffraction

X-ray diffraction is a method which identifies the crystalline phase of an unknown material being analyzed and also provide the geometry of the cell structure. The X-rays generated are filtered to produce monochromatic radiation in a parallel pattern focusing on the sample to be analyzed [64]. A constructive interference is produced when the X-rays incident with the sample satisfies the condition of the Braggs law given by

$$2d\sin\theta = n\lambda$$

The equation above relates the wavelength of the electromagnetic radiation with the crystal lattice spacing and the angle of the diffraction [64]. The X-rays scattered after incidence is been processed and analyzed. The powdered sample orientation is random, due to which all the diffraction pattern from the atomic arrangement in the crystal sample shall be attained when scanning through a range of Bragg's angle (2θ). The d-spacing in the sample obtained when converted from the diffraction peaks helps in identifying the sample by matching with the reference patterns in the software [64].

Above all, the main factor to be considered in the X-ray diffraction is the angle between the incidence and diffraction.

The average size of the crystalline structure of the catalyst can also be determined by X-ray diffraction. When analyzing the catalyst, the peaks showing intense and sharp diffraction tell us that the crystallite size is of long range order. If the peaks are broader then the size is below 100 nm [65]. Scherrer equation can be used to calculate the relationship between the peak broadening (B) at Braggs angle (2θ) and crystal size (L), as shown below

$$B\ (2\theta) = \frac{K\lambda}{L cos\theta}$$

The following figure shows the schematic of an X-ray diffraction instrument.
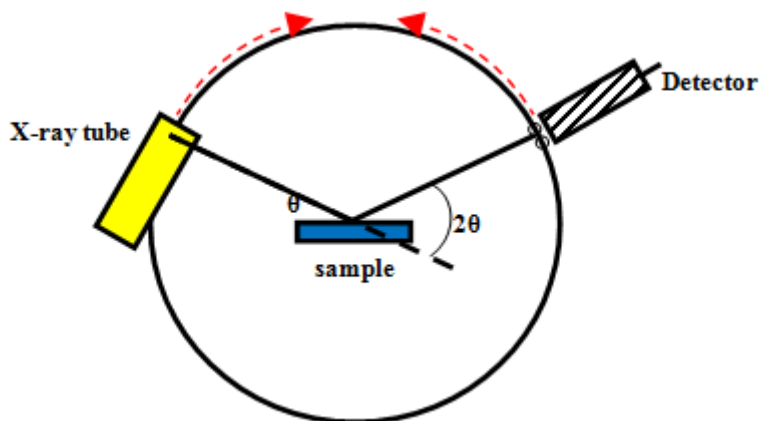
Figure 18: Schematic drawing of X-ray diffraction [31].

The figure shows the X-rays diffracted from the material is being analyzed by the diffractometer, which records the intensity with respect to the diffraction angle [31]. The filter is present to allow only the Kα radiations and suppress other radiation wavelength. This specific wavelength comes from the target material which is normally copper. The intensity of the diffracted X-rays striking the sample is been recorded when both the sample and detector are rotated. If this satisfies the Braggs equation then a peak is recorded. Goniometer is the device which controls the rotation of the sample with respect to the specified angle [64].

Siemens D500 Xray Diffractometer was used to record the diffraction pattern of the calcined catalysts at room temperature using CuKα Radiation ($\lambda=1.5418$Å). The analysis was performed from 20°-80° (2Θ, Braggs Angle) with step size of 1°/min.

2.2.6 Temperature Programmed Reduction

TPR is one of the most commonly used method to characterize the metal oxides catalysts. It analyzes the reducibility of the metal oxide's surface [66]. The reducing gas hydrogen (H_2) whose concentration is normally 3-17% is diluted in the carrier gas Argon. The composition of the reducing gas after the reduction is been measured using thermal conductivity detector (TCD).The signal from the TCD is converted to the concentration of the gas by calibration. The area under the peak generated in the plot between intensity (TCD signal) vs temperature (or time) yields the amount of H_2 gas consumed, and that also gives us an idea of the percentage of the active metal species being reduced. The equation can be shown as follows

$$MO \text{ (Metal Oxide)} + H_2 \longrightarrow M \text{ (Metal)} + H_2O \text{ (Water)}$$
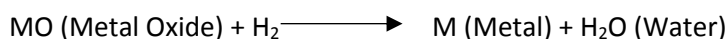
Parameters that affect the TPR profile are [31]

    i)   Heating Rate

    ii)   Flow rate of the reducing gas mixture

    iii)   Amount of reducible metal species present

    iv)   Concentration of H_2 in a carrier gas

Increasing the heating rate results in a faster increase of the temperature. As a consequence the reduction peaks of the sample appear at higher temperatures.

The maximum peak intensity in the plot shall indicate the maximum rate of reduction with respect to temperature. Figure 19 shows the schematic of the TPR set up.
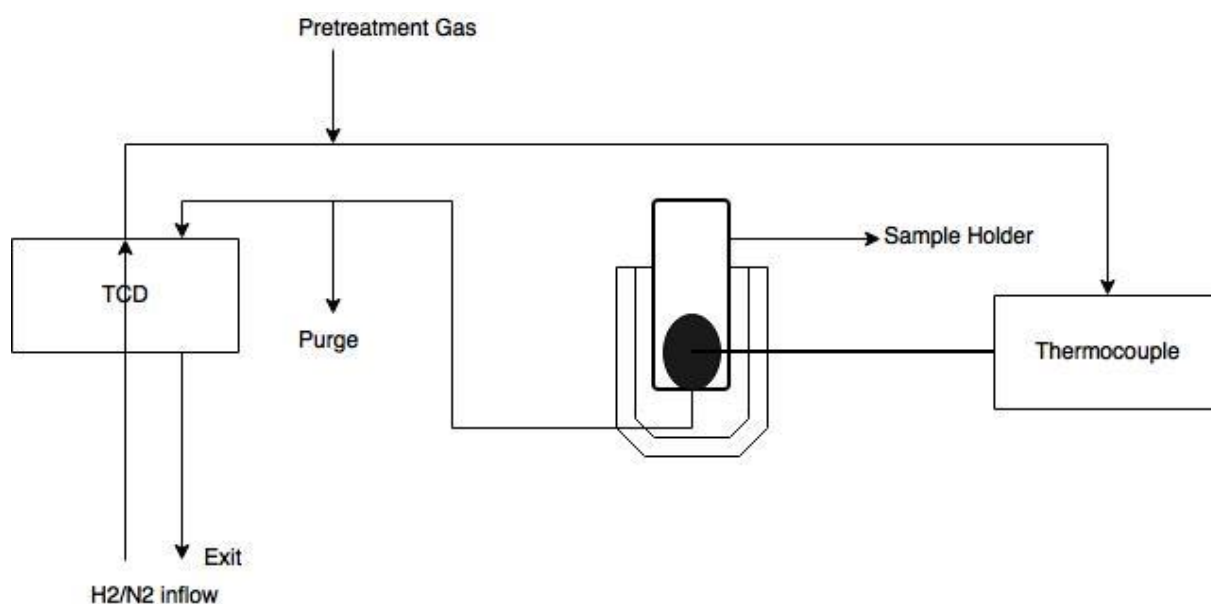
Figure 19: Basic schematic of the working of TPR[31]

TPR mainly gives information about the interaction of the metal species with the support and the reducibility of a catalyst.

Autochem II 2920 (Micromeritics) was used to perform the TPR analysis of the calcined catalysts. 10%H_2/Ar was flown over the catalyst at 50ml/min with a temperature ramp at 10 $^\circ$C/min from 100 to 950 $^\circ$C.

2.2.7 H₂ Chemisorption

Chemisorption is defined as a type of adsorption where chemical reaction takes place between the adsorbate gas and adsorbent through the formation of a chemical bond.

Chemisorption is very important in catalysis in terms of evaluating the active metal surface area exposed on the support. Dispersion and average particle size can be calculated respectively [67]. The catalytic activity depends on rate of chemisorption of reactant molecules and also the strength of the bond formed between adsorbate and adsorbent [68].

In H_2 chemisorption, hydrogen gas is used as an adsorbate gas to analyze the chemical interaction with the catalyst (adsorbent).When it interacts with the surface of a catalyst, normally 1 hydrogen molecule forms bond with 2 surface metal atoms. The reaction is shown as follows [31]

$$H_2 + 2M_s \rightarrow 2M_s - H$$
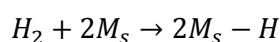
Where M_s is the surface metal atom.

The equation to evaluate dispersion of a metal on a support is as follows [31]

$$D = \left(\frac{Ns}{Nt} \right)$$

   Where N_s represents the total number of exposed metal atoms to the reactant molecules on the support, and N_t represents the total number of metal atoms present on the support.

Dispersion can also be calculated by [69, 70]:

$$D = \frac{Y}{\Sigma \frac{Wm}{Mm}} \times Fs \times 100\%$$

Where Y is the amount of H_2 chemisorbed (mol/g_{cat}); N_A is the Avogadro's constant   (6.023×10^{23} mol^{-1}), F_s is the stoichiometric factor (2 for H_2); W_m is the metal loading (g_m/g_{cat}) and M_m is the molar mass of Nickel (58.69 g/mol).

The active metal surface area per unit weight of the sample can be calculated by

   A_m (m²/gm) = (Total number of metal atoms on the surface) × (active metal cross sectional area)

$$\text{Or } A_m \text{ (m}^2\text{/gm)} = \frac{Y \times NA}{A} \times F_S$$

Where Y is the amount of H_2 chemisorbed (mol/g_{cat}), N_A is the Avogadro's constant (6.023×10^{23} mol^{-1}), F_s is the stoichiometric factor (2 for H_2) and A is the number of nickel surface atoms per unit area (m^{-2})

Static chemisorption technique was performed on original, oxidized and nitrogen doped CNT1020, CNT2040 and CNT4060 supported nickel catalysts.

ASAP 2020 Plus, Micromeritics was used to measure the metal dispersion and active metal area. Pretreatment was done to dry and remove the moisture of the catalysts using Helium gas. The temperature was ramped at 25 °C/min from ambient to 200 °C. The catalysts were then reduced to 400°C for 3 hrs at a rate of 10°C/min. This was followed by cooling to 35 °C at a rate of 10 °C/min.

2.3 Catalyst Activity Tests

For activity tests, 150 mg of CNTs supported nickel catalysts was loaded in a fixed bed reactor. The catalytic activity was evaluated at atmospheric pressure and at temperature of 350 °C.

Before conducting activity tests, pre-reduction of all the catalysts were carried out at 500°C for 3 hr by passing through 50% H_2 and 50% N_2 at a combined flow rate of 50 ml/min. After reduction and cooling to the reaction temperature of 350°C with 100% N_2, the gases were switched to mixture gases of 73.7% H_2, 18.8% CO_2 and 7.5% N_2 to a stoichiometric (H_2/CO_2) ratio of 4:1 at a total flow rate of 50 ml/min. N_2 is here added as an internal standard to calculate the outlet gas compositions. This gave required gas hourly space velocity (GHSV) of 20,000 ml/ (g_{cat}.h).

Calculation of Flow rate based on required GHSV

GHSV = 20,000 ml/ (g_{cat}.h) = 333.3 ml/(g_{cat}.min)

Samples Weighed = 150mg=0.150g

Total flow rate = $333.3 \dfrac{ml}{g \times min} \times 0.150$ g = 50 ml/min

The activity was carried out at 350 °C for 16 hr. The gas compositions and reaction conditions set for each catalysts activity test were defined in Table 6.

Table 6: Concentration and Flow conditions of the catalysts for activity tests

Catalysts	H$_2$(conc, %)	CO$_2$(conc,%)	N$_2$(conc, %)	Flow(ml/min)
Ni/CNT1020	73.7	18.8	7.5	50
Ni/OCNT1020	73.7	18.8	7.5	50
Ni/NCNT1020	73.7	18.8	7.5	50
Ni/CNT2040	73.7	18.8	7.5	50
Ni/OCNT2040	73.7	18.8	7.5	50
Ni/NCNT2040	73.7	18.8	7.5	50
Ni/CNT4060	73.7	18.8	7.5	50
Ni/OCNT4060	73.7	18.8	7.5	50
Ni/NCNT4060	73.7	18.8	7.5	50

Table 7: Reaction Conditions for CO$_2$ Methanation.

Catalyst amount	150 mg
Reduction temperature	500 ^{o}C
Reduction H2/N2 ratio	1:1
Reaction temperature	350 ^{o}C
Pressure	1 atm
H$_2$/CO$_2$ ratio	4:1
GHSV(Gas hourly space velocity)	20,000 ml/(g$_{cat}$.h)

The outlet product gas stream was analyzed by Agilent 7890B Online Gas Chromatograph Analyzer equipped with 2 thermal conductivity detectors (TCD). CO$_2$ conversion and CH$_4$ selectivity were calculated as follows[71]:

$$X_{CO2} = \frac{F_{co2,in} - F_{co2,out}}{F_{co2,in}} \times 100\%$$

$$S_{CH4} = \frac{F_{ch4,out}}{F_{co2,in} - F_{co2,out}} \times 100\%$$

Figure 20 shows the flow chart of the CO$_2$ methanation setup.
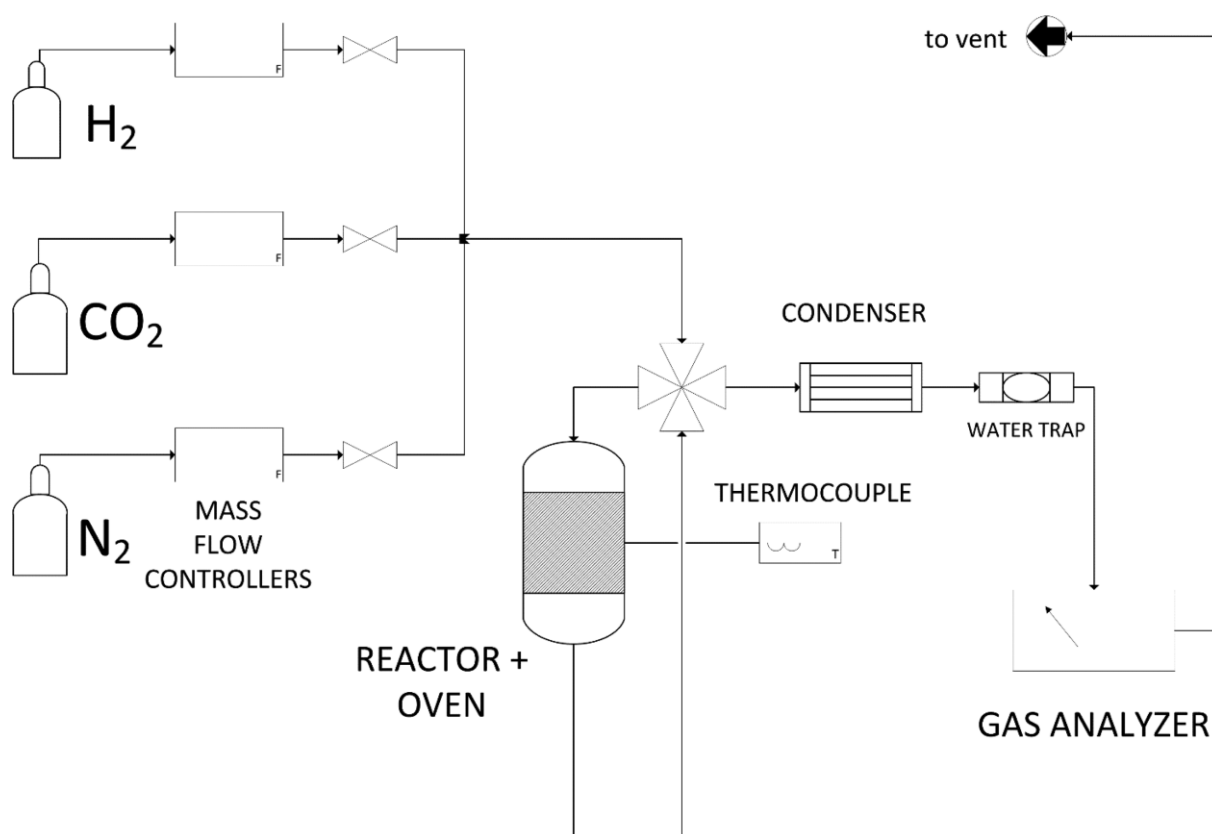
Figure 20:CO$_2$ Methanation Setup [19].

CO$_2$, N$_2$ and H$_2$ gases are mixed proportionally by mass flow meters [19]. The fixed bed reactor with the sample holder is placed inside the oven which is controlled by the PID. In order to measure the reaction temperature, a thermocouple is placed on the top of catalyst bed vertically [19]. As water is formed as a byproduct during the methanation reaction, the outlet gas stream after the reactor is passed through a condenser so that the water is trapped and removed. The composition of the mixture of gases at outlet is measured for each run.

Chapter 3: Results and Discussions

3.1 Fourier Transform Infrared Spectroscopy

In order to investigate the presence of surface functional groups, FTIR characterization of the original, oxidized and nitrogen doped CNTs were carried out with the CNT-2040 samples. The FTIR spectra of different samples are presented in Figure 21.

In Figure 21, the spectra at 3430 cm^{-1} attributed to the presence of the O-H or the carboxylic groups generating stretching vibrations on the surface of the CNT. It was found for both the original and the functionalized CNTs, and this mainly comes from absorption of water from the environment [42]. The spectra around 2850 and 2900 cm^{-1} attributed to the stretching vibration of the -CH_2 groups which are asymmetric and symmetric respectively [42]. The bands observed at 1530 and 1630 cm^{-1} attributed to the presence of carboxylic groups, aromatic and unsaturated structure of -C=C- bonds. The peaks were less intensive for the functionalized CNTs compared to original ones [42]. The peaks at 1250 cm^{-1} ascribed to the presence of C-O groups on the tubular structures. The intensity of the peak at this wavelength increased a lot with the functionalization of CNTs. The intensity decreased in nitrogen doped CNT where on introduction of nitrogen atoms, the oxygen containing functional groups partly decomposed on the walls of CNT. But no peaks of Nitrogen containing groups could be identified for the nitrogen doped CNTs, probably due to the ineffectiveness of the chosen reaction conditions during the post treatment with ammonia.
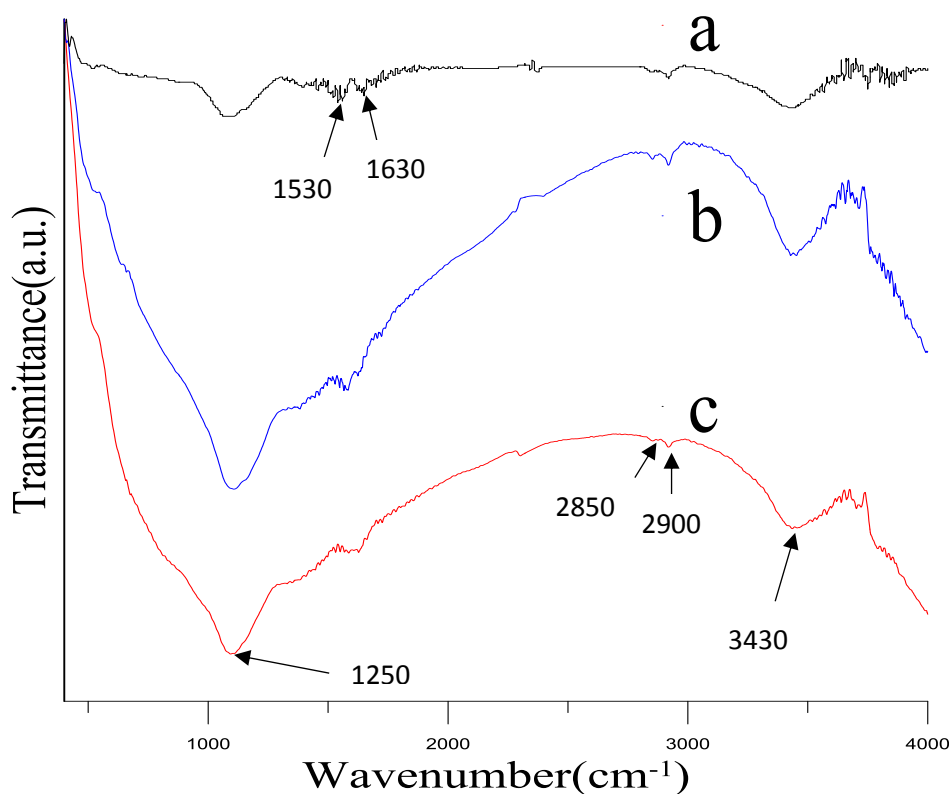
Figure 21: FTIR analysis of as received and functionalized CNTs; a) original CNT, b) oxidized CNT, c) nitrogen doped CNT.

3.2 Raman Spectroscopy

In order to study the structural disorder or defect on the walls of CNTs on functionalization and the original sample, Raman characterization were carried out on original, oxidized and nitrogen doped CNT2040 samples. As shown in Figure 22, the two main peaks in the Raman spectra observed at 1376 cm^{-1} and 1576 cm^{-1} attributed to the D-band and G-band. The presence of amorphous carbon and structural disorder and defects in tubes with foreign atoms were indicated by the D-band and the degree of crystallinity are given by the G-band The other peaks at 2700, 2900 and 3300 cm^{-1} were attributed to the multiple splitting of G-band which indicated the interaction between the layers of the exterior walls of the CNTs [42].

The intensity ratio (I_d/I_g) indicated the structural disorder or defects in the tubes on functionalization with oxygen and nitrogen functional groups. Compared with the original sample, the oxidized CNTs showed lower I_d/I_g ratio, indicating more disorder or defects in the oxidized CNTs, which was as expected. However, further treatment of the OCNTs actually made the sample more ordered, which

was even higher than the original CNT. At this point we were not clear of the increase of the order after further Nitrogen treatment. In literature the increase in the intensity ratio in nitrogen doped case has been explained by the alteration in the tubes and transformation of sp^2 hybridization to sp^3 hybridization of the carbon atoms in the graphene layer [42].
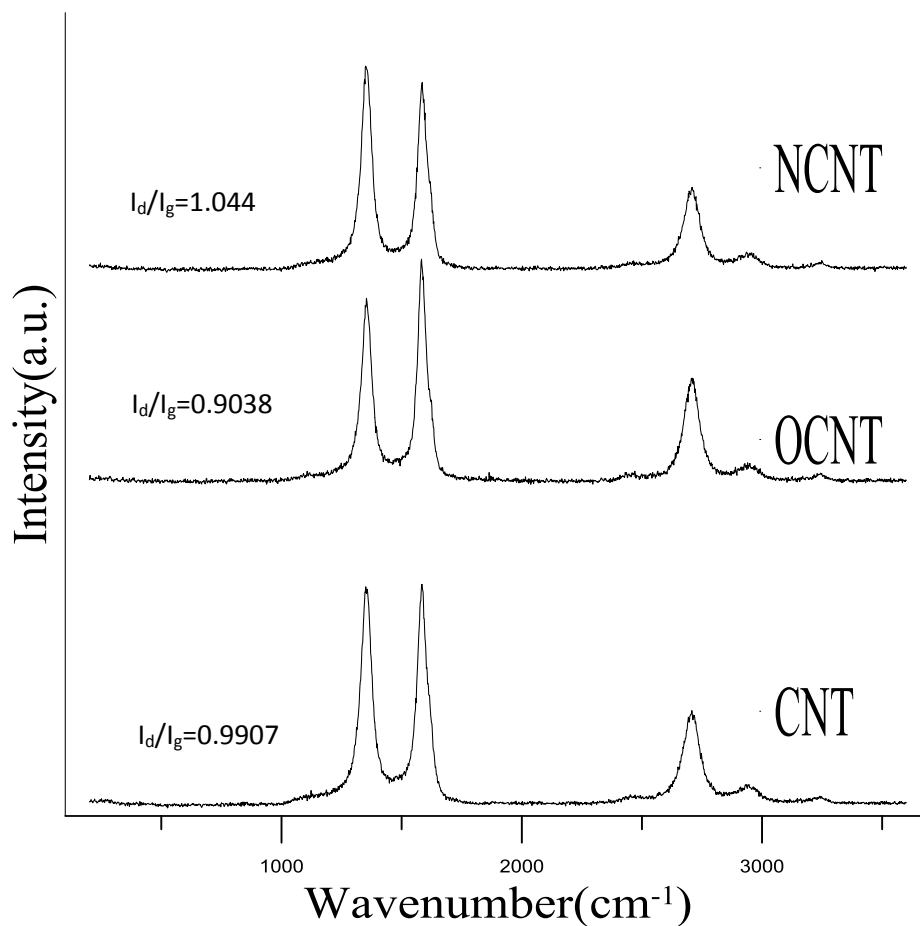
Figure 22: Raman analysis of the original and functionalized CNT2040.

3.3 Thermogravimetric Analysis (TGA)

TGA analysed the thermal stability of CNTs, which in turn can gave an indication of the structural order of the original, oxidized and nitrogen doped CNTs [42]. The samples analyzed here were again CNT2040, OCNT2040, and NCNT2040. Figure 23 showed the weight loss with temperature increase on heating different CNTs.

It showed the oxidation of the original CNTs starting from 580 ^{o}C and ending with a maximum weight loss rate at 720 ^{o}C. Oxygen doped CNTs also showed a similar trend with a slightly lower starting temperature of weight loss but a higher ending weight loss temperature of 740 ^{o}C. This could be ascribed to that the CNTs refluxed with acid removed the amorphous carbon and metallic residual catalysts from the tube, even though surface oxygen groups were introduced. However the functionalization of CNTs with nitrogen atoms showed lower thermal stability than the original and the oxidized ones. This difference attributed to the introduction of defects when nitrogen heteroatoms were further doped on it [42]. However, overall the oxidation profile between the three samples were not very different, and
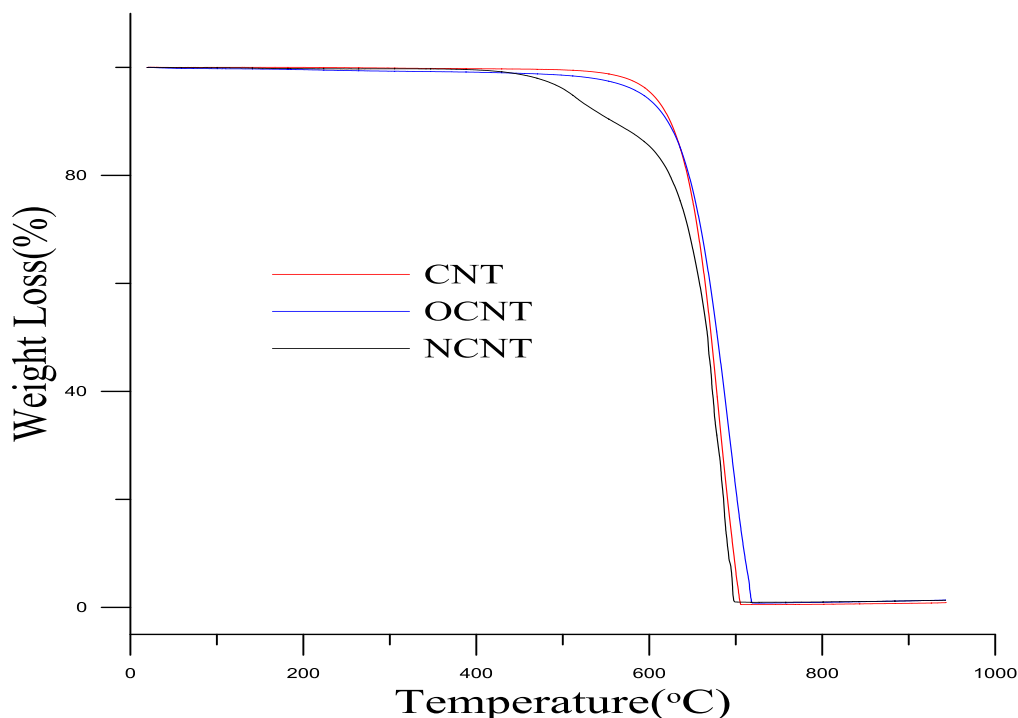
Figure 23: TGA analysis of different CNTs.

not much difference in thermal stability could be observed after the functionalization.

Table 8 shows the final weight loss after the TGA analysis.

Table 8: Weight loss of Original and Functionalized CNTs during TGA analysis

Carbon samples	Weight loss (%)
CNT	99.1
OCNT	98.6
NCNT	98.8

Not much difference in thermal stability could be observed after the functionalization. This could be attributed to the discrepancy in setting the right process conditions when the tubes were functionalized especially.

3.4 N_2 Physisorption

The N_2 physisorption characterization was performed for the original and oxygen doped sample. The BET adsorption isotherm plot to determine the specific surface area and the BJH isotherm plot to determine pore size distribution for the original and oxidized CNT1020, CNT2040, and CNT4060 samples were presented as in Figure 24 (a)-(c)
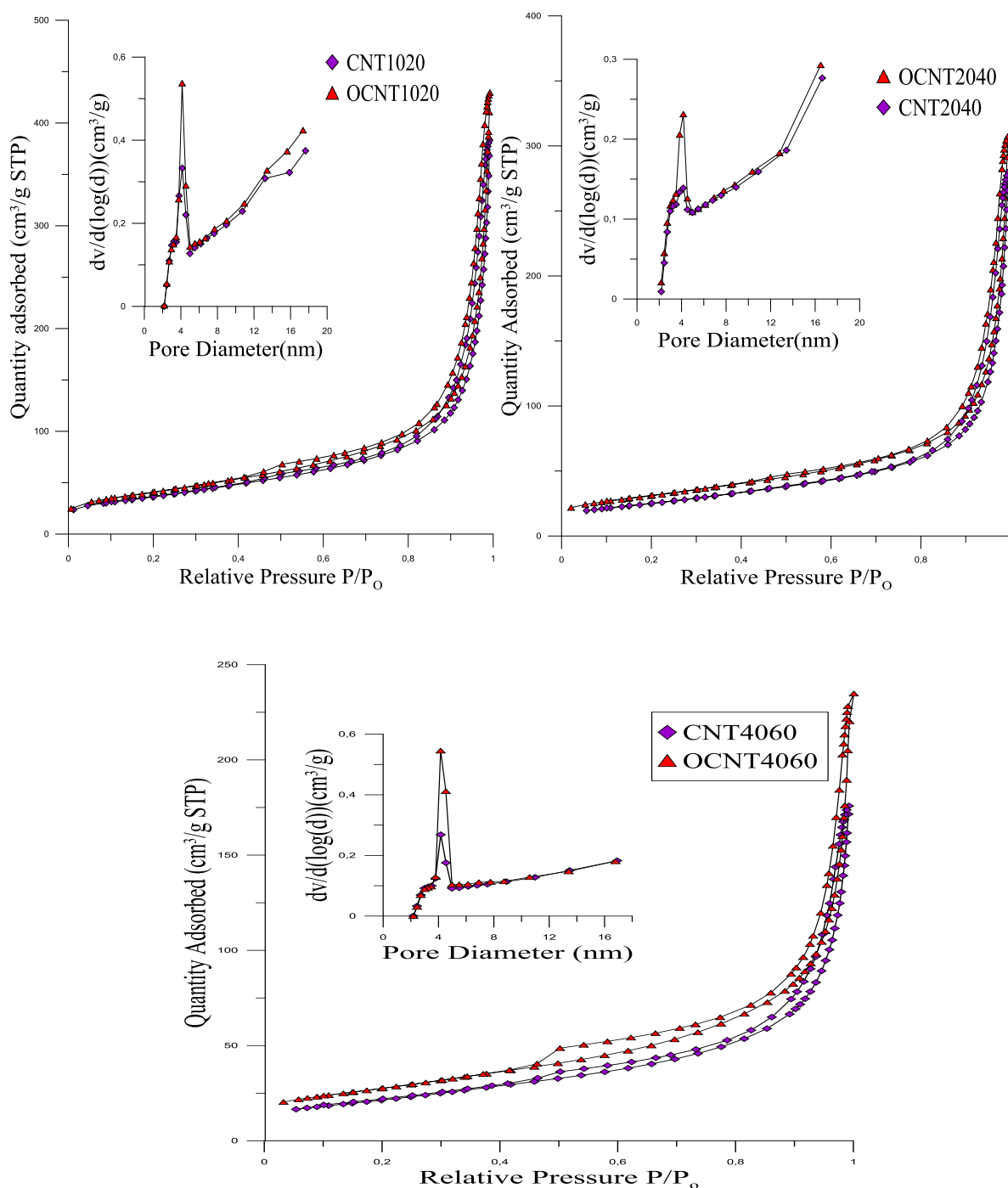
Figure 24: BET adsorption isotherm and BJH pore size plot of the oxidized and original CNTs (a) CNT1020, (b) CNT2040, (c) CNT4060.

 All BET adsorption showed the type IV isotherm. As summarized in Table 9, when we compare the carbon samples oxidized with the original samples, the specific surface area were increasing with for all oxidized CNTs. This was mainly due to that after refluxing with nitric acid, the metal and amorphous carbon impurities which blocked the pores were removed, resulting in an increase in surface area [72-75].

Figure 24 (a)-(c) also gave the pore size distribution of the oxidized and original carbon nanotubes of different diameters (CNT1020, 2040 and 4060). As we can see all the CNTs only have mesopores. Table 9 showed that in all cases after oxidation the pore volumes increased slightly, while the average pore diameters decreased slightly. It was also clear while the average diameter of the CNTs decreased, both the BET surface area and the pore volume increased. Therefore, a smaller diameter of CNTs was preferred as support for catalyst preparation.

Table 9: Textural Properties of the CNTs supports.

Samples	Surface area (m^2/g)	Pore Volume (cm^3/g)	Average Pore size (nm)
CNT1020	130.6	0.21	6.72
OCNT1020	145.2	0.23	6.52
CNT2040	90	0.14	6.62
OCNT2040	109.4	0.15	6.38
CNT4060	77.6	0.12	6.17
OCNT4060	98	0.14	5.79

The N_2 adsorption for the calcined Ni impregnated catalysts had been measured for comparison, and the results were shown in Table 10. When we compare the BET surface areas of the CNT supports and the impregnated catalysts, there was a slight increase in surface area and pore volume of the impregnated CNTs, even though the change was small. Normally when a metal precursor was impregnated on the support, the surface area should have been lower because the metal occupied the surface and pore structure. We were not clear how the surface area and pore volume increased after Ni impregnation. Probably the CNT supported catalysts after calcination developed better porosity in the CNTs due to a high calcination temperature of 500 °C, which burned off some of the CNT structures.

Table 10: Textural Properties of the Calcined Catalysts.

Calcined Catalysts	Surface area (m^2/g)	Pore Volume (cm^3/g)	Average Pore size (nm)
Ni/CNT1020	141.1	0.22	6.47
Ni/OCNT1020	158.1	0.22	5.97
Ni/CNT2040	107.7	0.16	6.27
Ni/OCNT2040	120.6	0.17	6.04
Ni/CNT4060	98.3	0.14	6.02
Ni/OCNT4060	105.9	0.15	6.00

3.5 X-Ray Diffraction

The calcined catalysts were subjected to XRD characterization to study the crystalline phases and particle sizes of nickel oxides. The diffraction patterns of the nickel oxide supported on original, oxidized and nitrogen doped CNTs of different diameters CNT1020, CNT2040, CNT4060 were shown in Figure 25, 26 and 27.
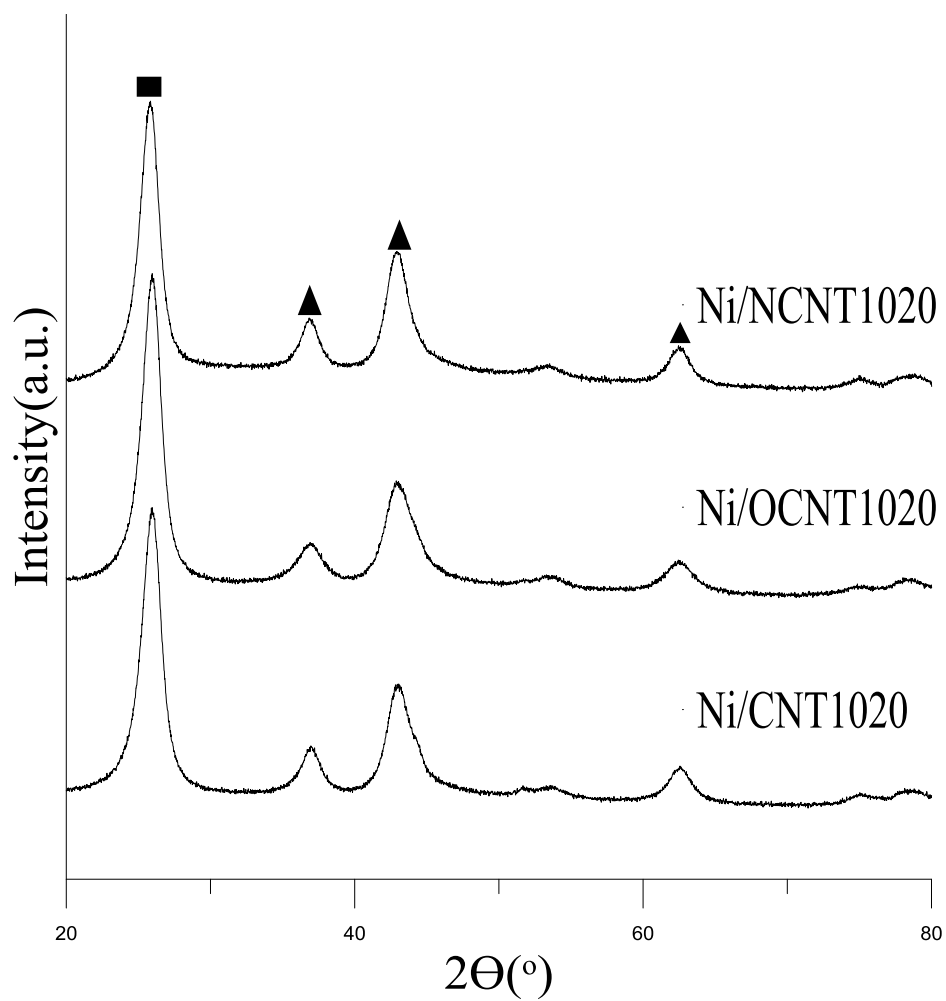
Figure 25: XRD Patterns of the CNT1020 supported Catalysts, ■ - carbon, ▲ - nickel Oxide.
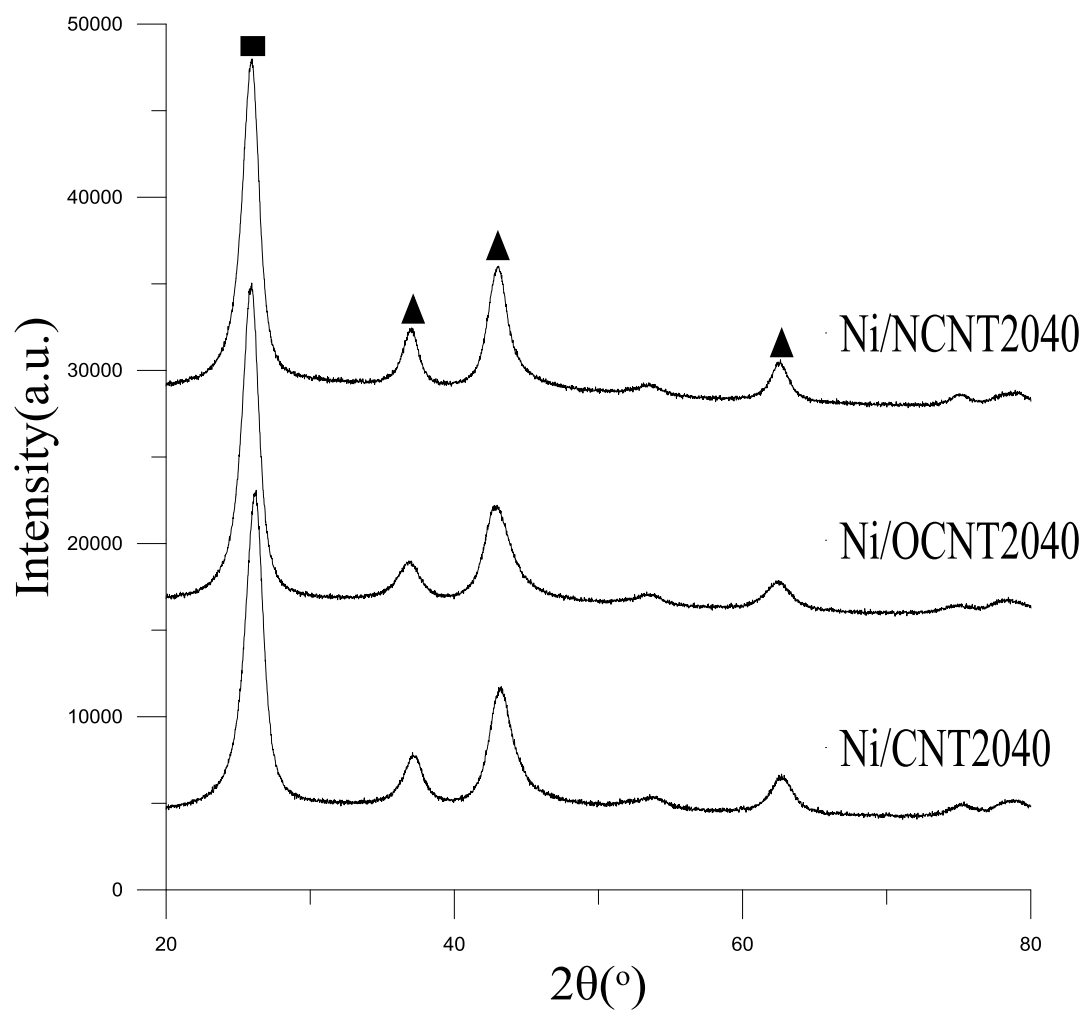
Figure 26: XRD Patterns of CNT2040 Supported Catalysts, ■ - carbon ▲ - nickel Oxide.
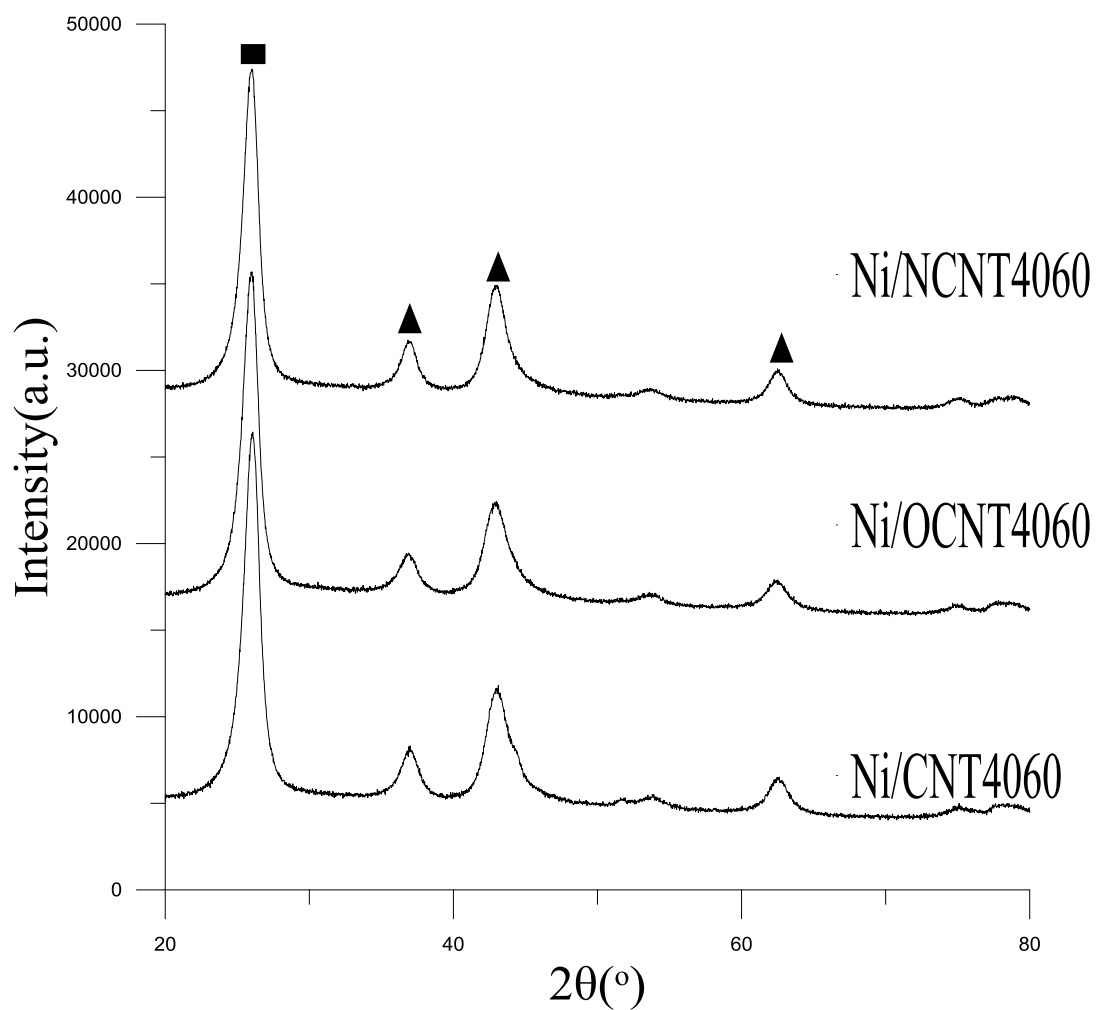
Figure 27: XRD patterns of CNT4060 supported catalysts, ■- carbon ▲- nickel oxide.

In Figures 25-27, the same diffraction peaks at 26°, 38°, 44° and 64° for all the CNT supported catalysts were observed. The diffraction peak at 26° attributed to the CNT phase. The diffraction peaks at 38°, 44° and 64° attributed to the presence of nickel oxide. The particle size of the nickel species in the catalyst were calculated by the Scherrer equation and were summarized in table 11.

Table 11: Particle size of the CNT supported catalysts.

Catalysts	NiO Particle size(nm)
Ni/CNT1020	4.7
Ni/OCNT1020	4.2
Ni/NCNT1020	5.3
Ni/CNT2040	5.2
Ni/OCNT2040	4.8
Ni/NCNT 2040	6.1
Ni/CNT4060	5.3
Ni/OCNT4060	5.2
Ni/NCNT 4060	6.0

The particle size of all CNT supported nickel oxide species were less than 10 nm. Even though by calculation the particle sizes were slightly different, the values were probably all indifferent and within experimental error. This was also observed from the peak intensities in Figures 25-27, for NiO (Nickel Oxide) the peak intensities were very similar. A not-so-obvious trend from Table 11 was that it seemed like the decrease of CNT diameter gave slightly smaller NiO particle size, but more detailed quantitative analyses was needed to be performed to support the conclusion.

3.6 Temperature Programmed Reduction

To investigate the reducibility of the different catalysts, temperature programmed reduction was performed on all the calcined CNT supported catalysts. Figure 28, 29 and 30 showed the reduction behavior trend of original, oxidized and nitrogen doped CNT1020, CNT2040, CNT4060 supported catalysts, respectively.
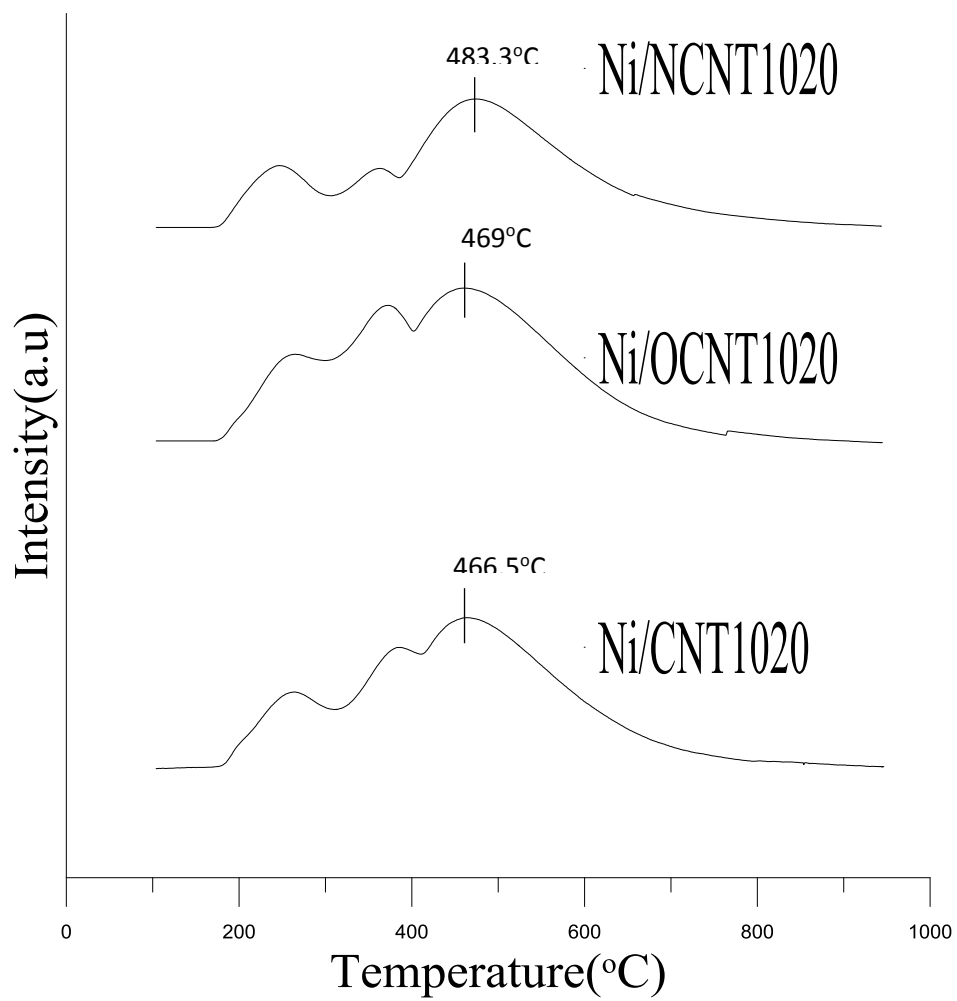
Figure 28: TPR profile of the CNT1020 supported catalysts.
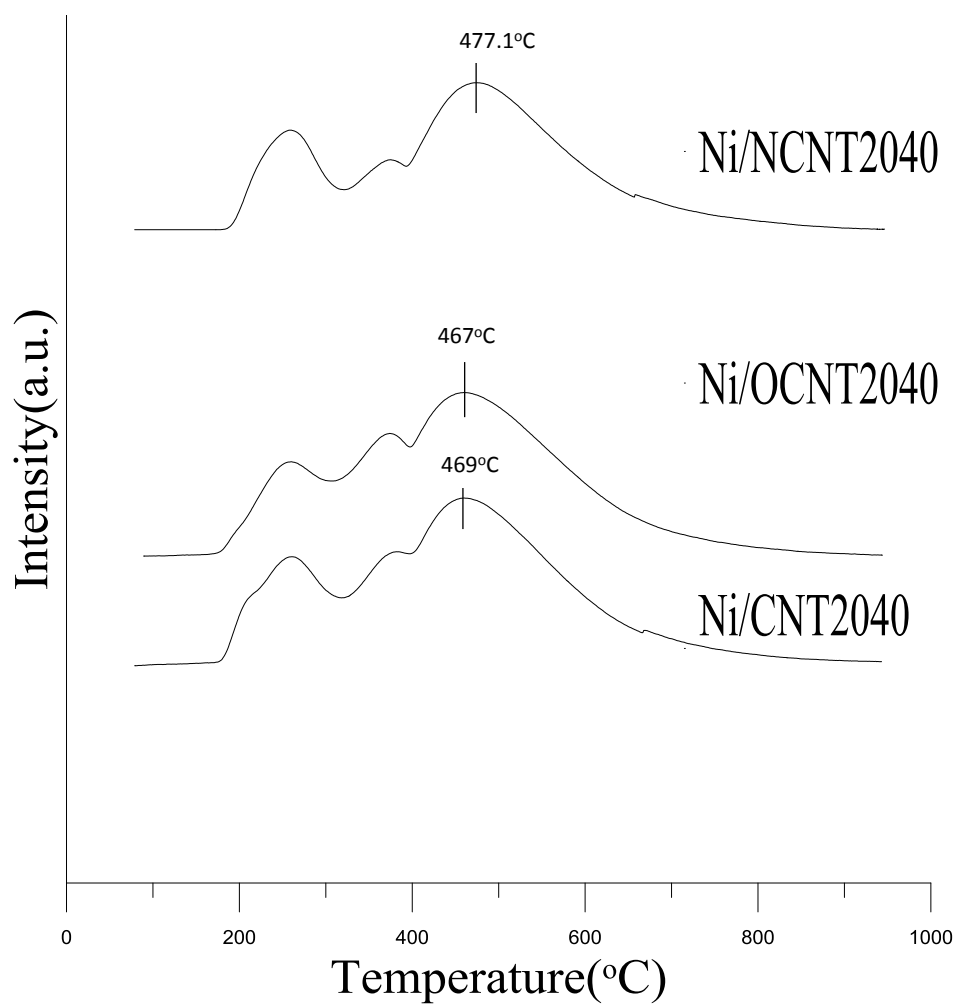
Figure 29: TPR profile of CNT2040 supported catalysts.
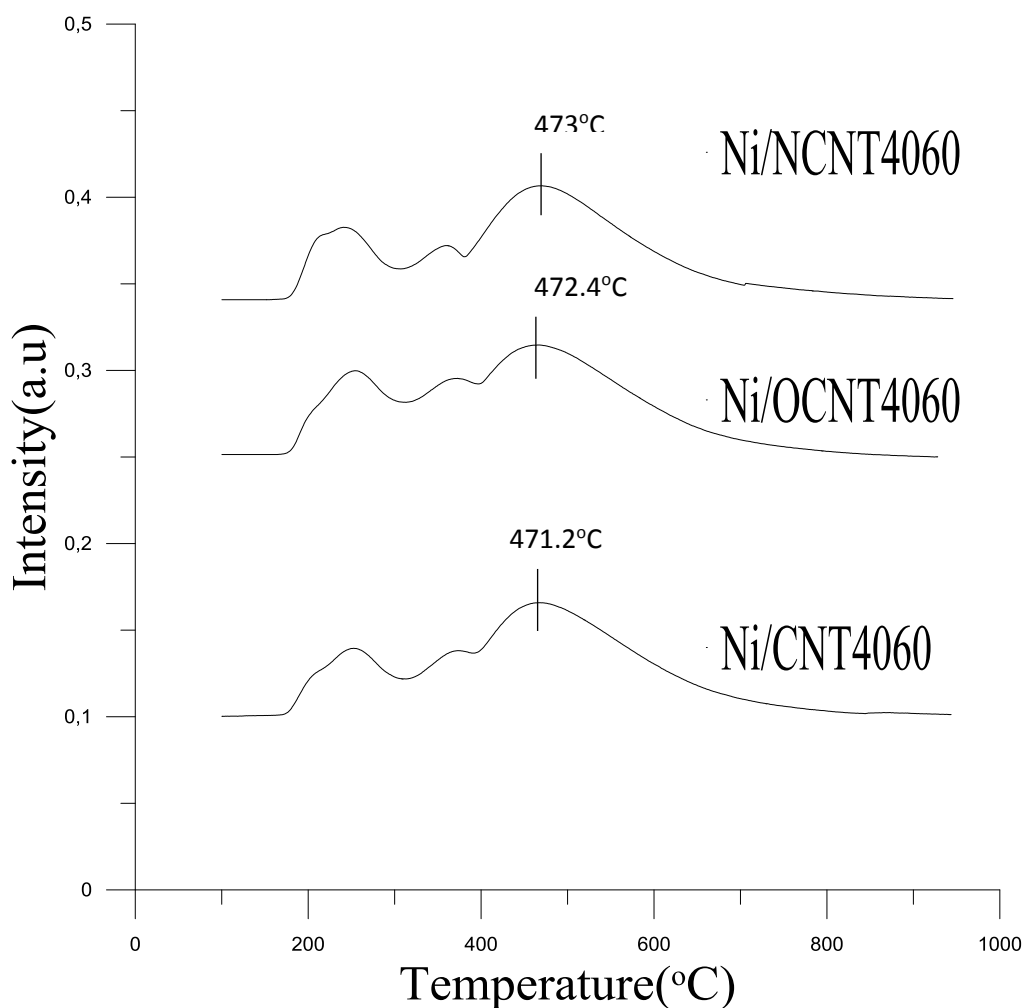
Figure 30: TPR Profile of CNT4060 supported catalysts.

Three reduction peaks was observed for all CNTs support Ni catalysts. It can be further seen that only slight shift in the maximum reduction temperature was observed for the different CNTs supported catalysts. The reduction peaks found at around 250 °C could be potentially attributed to the overflow effect of hydrogen which activated hydrogen molecules to promote a reduction reaction between nickel species and hydrogen at low temperatures [15]. The high temperature peak at around 350 °C was probably due to the gasification of CNT by H_2. The maximum reduction peak temperature, as shown in Figures 28-30, all happened at around 480 °C. The peak was obviously the reduction of NiO to metallic Ni. The small shift in the maximum reduction peak temperature was difficult to explain, but it showed similar reducibility of all CNTs supported Ni catalysts.

3.7 H$_2$ Chemisorption

We further performed H2 chemisorption of the CNT2040 supported catalysts. The results were shown in Table 12.

Table 12: Chemisorption analysis of the catalysts.

Catalysts	H$_2$ uptake (cm^3/g$_{cat}$)	Dispersion (%)	Metallic Surface Area (m^2/g of catalyst)
Ni/CNT2040	0.329	1.14	1.46
Ni/OCNT2040	1.323	4.62	5.88
Ni/NCNT2040	0.202	0.71	0.90

It was clear from the chemisorption study that a large increase in dispersion and active metal area were obtained for the oxidized CNT supported catalyst when compared with original CNT support catalysts. This was attributed to increase in surface area of CNTs on refluxing with acids which thereby resulted in the increase in dispersion. Further treatment with N doping on the CNTs on the contrary decreased significantly of the metal dispersion and metallic surface area. Therefore, Nitrogen doping was not beneficial for preparing supported Ni catalysts with high dispersions on CNTs.

3.8 Catalyst Activity Tests

We compared the activity of different catalysts at exact the same reaction conditions for CO$_2$ methanation. Activity tests of each sample were performed for about 16 hr to evaluate the difference with respect to conversion and selectivity with time on stream of the original, oxidized and nitrogen doped CNT supported catalysts.
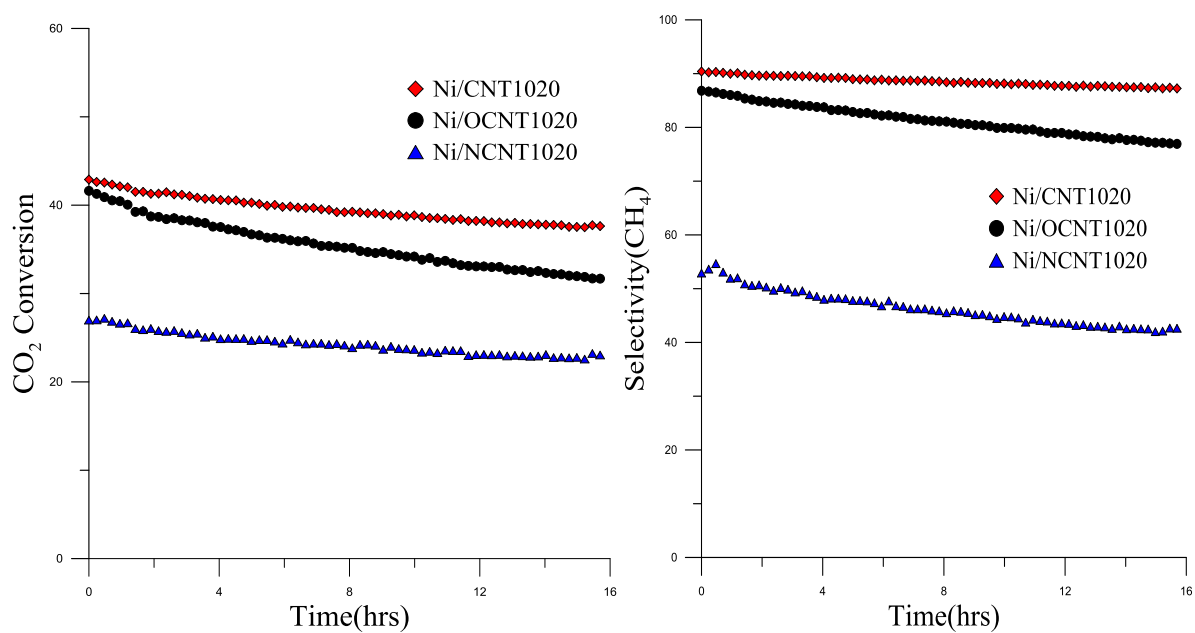
Figure 31: CO$_2$ conversion and CH$_4$ selectivity of original, oxidized and nitrogen doped CNT1020 supported Ni catalysts.
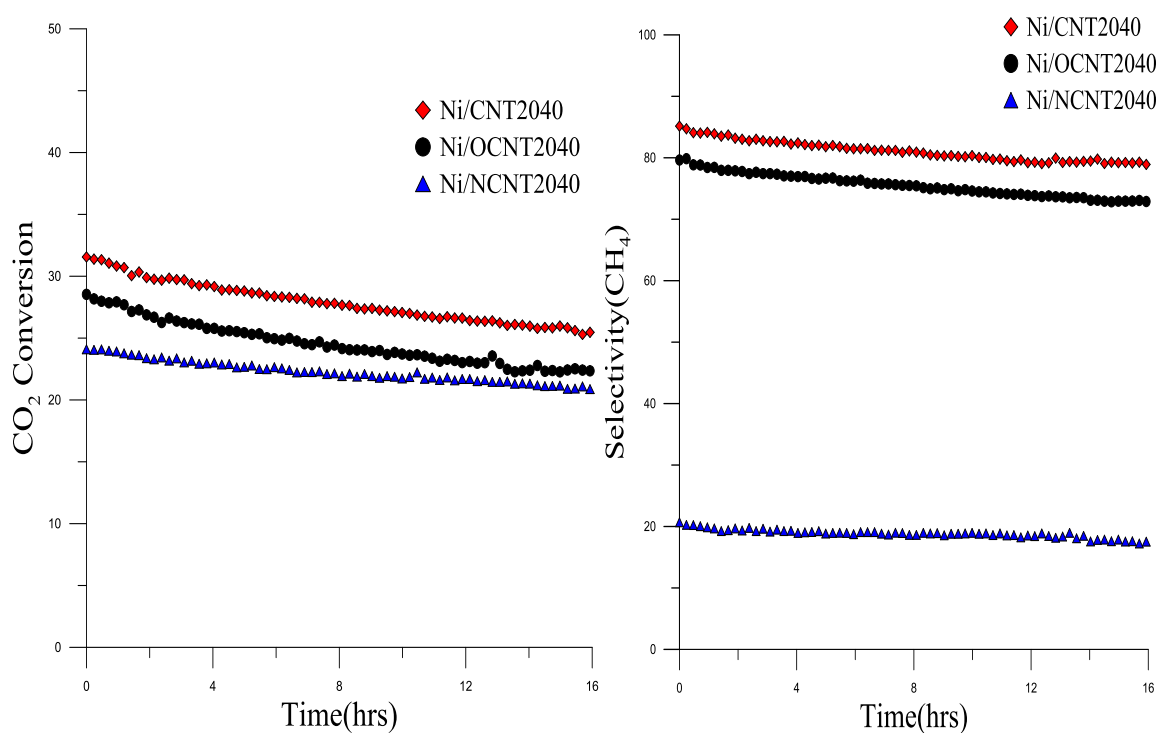
Figure 32: CO$_2$ conversion and CH$_4$ selectivity of original, oxidized and nitrogen doped CNT2040 supported Ni catalysts.
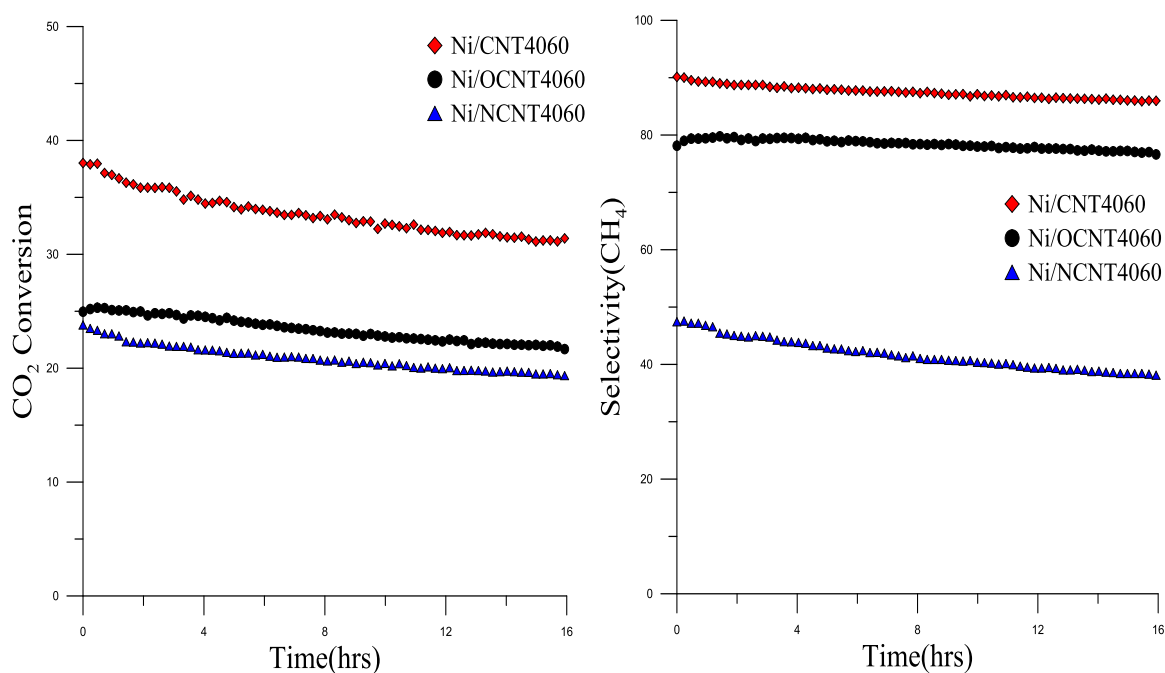
Figure 33: CO₂ conversion and CH₄ selectivity of original, oxidized and nitrogen doped CNT4060 supported Ni catalysts.

The CO_2 conversion and CH_4 selectivity of the CNT1020, CNT2040 and CNT4060 for the oxygen doped, original and nitrogen doped supported catalysts were presented in Figures 31, 32 and 33. All the three catalysts showed a deactivation trend throughout the time on stream. For clarity, the values for initial and end CO2 conversion, initial CH4 selectivity have been summarized and presented in Table 13. The data did not give a very clear trend for comparison. However, some general observation and trends could be summarized.

Taking CNT 1020 as an example, the Ni/CNT1020 catalyst showed the initial CO_2 conversion of 44%, and deactivated to 40% after 16 hr on stream. The Ni/OCNT1020 catalyst had initial and end conversions of 42% and 34%, while the Ni/NCNT1020 catalyst had 28% and 25%, respectively. The CNT2040 catalysts showed a similar behavior with activity in the order of Ni/CNT2040 > Ni/OCNT2040 >Ni/NCNT2040, with initial CO_2 conversion of 33%, 28%, and 24%, respectively. As can be seen in Table 13, the CNT4060 supported catalysts also presented the same trend, although the magnitude of the activity difference showed large divergence.

Obviously, the original CNT supported catalysts had higher activity compared with the OCNT support ones, which in turn had higher activity than the NCNT supported catalysts. This was contradictory with chemisorption study presented in section 3.7. However, taking into consideration that the OCNT had more surface oxygen containing groups such as –OH or –COOH, it might have not influenced both CO_2 and H_2 adsorption to take place. Therefore, even though OCNT had higher surface area and indeed higher dispersion of Ni, the catalysts were not beneficial for CO_2 methanation.

For the NCNT supported catalysts, as shown by FTIR study there was no clearly observable Nitrogen containing groups on the CNT surface but reduced amount of oxygen containing functional groups indicated small quantities of N containing groups would be present on the CNTs. It was possible that further Nitrogen treatment would not improve CO_2 adsorption, but on the other hand further reduced the surface area of NCNT, was shown by chemisorption study in Table 12. In the end, the NCNTs supported catalysts gave the worst performance for CO_2 methanation.

Another not so obvious trend was that decreasing of the CNT diameter in general resulted in an increase of the CO_2 conversion. This was explained by the fact that the CNTs with smaller diameters had higher surface area, which gave smaller Ni particle sizes. The confinement effect of the smaller diameter CNTs might have contributed to a smaller Ni particle sizes in the supported catalysts.

In terms of CH4 selectivity, it was clear for CNTs with different diameters, the CH_4 selectivity was in the order of Ni/CNT > Ni/OCNT > Ni/NCNT. This could be ascribed to the fact that the doping of oxygen decreased H_2 adsorption capacity on the catalyst surface, which therfore gave lower conversion to CH_4 but increased the conversion to CO. This was proved by the fact that the functionalized CNTs always produced more CO as observed by GC.

It would be interesting to compare the CNTs supported Ni catalysts for CO_2 methanation to the Al_2O_3 supported catalysts [76]. For Ni/Al_2O_3 catalyst, the CO_2 conversion was much higher at similar reaction condition, while the CH_4 selectivity was close to 100%. Therefore, it seemed like CNTs was not a promising support for Ni based CO_2 methanation catalysts.

It could also be mentioned that all our Ni/CNTs catalysts had been reduced at 500^oC, which was probably too high a temperature for the reduction of Ni/CNT catalysts and as a consequence led to their bad performance.

Table 13 showed the Activity results of original, oxidized and nitrogen doped carbon nanotubes supported nickel catalysts tested for CO_2 methanation.

Table 13: CO_2 conversion and CH_4 selectivity of the original, oxidized and nitrogen doped CNTs supported Ni catalysts.

Sample Name	CO₂ conversion (Initial)	CO₂ conversion (Final)	Deactivation	CH₄ selectivity (Initial)
Ni/CNT1020	43%	40%	7.0%	91%
Ni/OCNT1020	42%	35%	16.6%	84%
Ni/NCNT1020	27%	24%	11.1%	54%
Ni/CNT2040	33%	27%	18.1%	84%
Ni/OCNT2040	28%	24%	14.2%	80%
Ni/NCNT2040	24%	22%	8.3%	22%
Ni/CNT4060	38%	34%	10.5%	90%
Ni/OCNT4060	25%	23%	8.0%	80%
Ni/NCNT4060	24%	21%	14.2%	48%

Chapter 4: Conclusion and recommendations for future work

In this study CNTs with different inner and outer diameters were used to prepare Ni based catalysts for CO_2 methanation. The CNTs were treated by refluxing in concentrated nitric acid and ammonia treatment to compare the effect of oxygen and nitrogen doping on CNT supported Ni catalyst performance for CO_2 methanation. Selected CNTs supports and Ni catalysts were characterized by N_2 physisorption analysis, XRD, H_2 chemisorption, TPR, FTIR, Raman Spectroscopy and TGA in order to evaluate and correlate the catalyst structure with their catalytic performance in CO2 methanation. The following results were concluded or deduced from this study:

i) FTIR showed oxygen being successfully introduced onto the surface of the CNTs, while treatment with ammonia was less successful with no obvious Nitrogen containing groups observed. Raman spectroscopy showed a slight higher intensity ratio of the nitrogen doped CNTs than the original CNTs, indicating potentially less defects on the CNTs by functionalization with nitrogen atoms. The oxidized CNTs showed a lower intensity ratio than the original ones. The TGA analyses however showed that the thermal stability of the CNTs were of a similar manner.

ii) BET analysis demonstrated some increase of the surface area of the calcined Ni catalysts compared with the CNTs, which was probably due to the fact that calcination at 400 ^{o}C in the presence of Ni had destructed the CNT structure somehow and developed porosity in the CNTs.

iii) XRD study gave similar peak intensity and NiO particle sizes as calculated by Scherrer equation, and the particle sizes were all below 10 nm.

iv) TPR showed only small difference in the reduction pattern and reducibility of the different CNTs support Ni catalysts.

v) H_2 chemisorption analysis demonstrated that oxygen doping resulted in supported Ni catalysts with the highest dispersion and metallic surface area.

The CO_2 methanation activity had been evaluated in a fixed bed reactor. It was found that the Ni catalysts supported on original CNTs showed higher activity than the oxidized CNTs, which in turn was higher than the nitrogen doped CNTs. This was explained by doping with oxygen resulted in lower CO_2 and H_2 adsorption capacity on the catalysts, while the doping with Nitrogen in this study was not effective and did not result in higher CO_2 adsorption capacity. This was further supported by the fact that the original CNTs supported Ni

catalyst also presented the highest CH_4 selectivity in all cases, because the doped catalysts gave higher CO selectivity due to the inability to adsorb H_2. The maximum CO_2 conversion was >40% during 16h time or stream on the Ni/CNT1020 catalyst, which also gave the highest CH_4 selectivity of 91%.

The following ideas can be followed to further improve the performance of the CNTs supported Ni catalysts for CO_2 methanation in the future work:

i)   Changes in the preparation method such as deposition-precipitation could be tried to improve Ni dispersion of metal species on the CNT supports. Oxygen has a negative effect for CO_2 methanation, therefore the CNTs is to be avoided to be functionalized by oxygen, while effective nitrogen doping could be implemented to increase the surface Ni containing groups to improve CO_2 adsorption.

ii)   In order to prevent gasification of CNTs during activity tests, calcination and reduction of the catalysts should be performed at lower temperatures ($300 - 350\ ^{\circ}C$).

iii)   Addition of promoters like cerium and lanthanum to the catalysts could be beneficial in order to increase the rate of conversion and stability.

Bibliography

1. Fechete, I. and J.C. Vedrine, *Nanoporous materials as new engineered catalysts for the synthesis of green fuels.* Molecules, 2015. **20**(4): p. 5638-5666.
2. Gao, J., et al., *A thermodynamic analysis of methanation reactions of carbon oxides for the production of synthetic natural gas.* RSC Advances, 2012. **2**(6): p. 2358-2368.
3. Council, N.R., *America's energy future: technology and transformation*. 2010: National Academies Press.
4. Statistics, I., *CO2 emissions from fuel combustion-highlights.* IEA, Paris http://www. iea. org/co2highlights/co2highlights. pdf. Cited July, 2011.
5. Birol, F., *World energy outlook 2010.* International Energy Agency, 2010. **1**.
6. Centi, G. and S. Perathoner, *Opportunities and prospects in the chemical recycling of carbon dioxide to fuels.* Catalysis Today, 2009. **148**(3): p. 191-205.
7. Wang, W., et al., *Recent advances in catalytic hydrogenation of carbon dioxide.* Chemical Society Reviews, 2011. **40**(7): p. 3703-3727.
8. Wei, W. and G. Jinlong, *Methanation of carbon dioxide: an overview.* Frontiers of Chemical Science and Engineering, 2011. **5**(1): p. 2-10.
9. Brooks, K.P., et al., *Methanation of carbon dioxide by hydrogen reduction using the Sabatier process in microchannel reactors.* Chemical Engineering Science, 2007. **62**(4): p. 1161-1170.
10. Sabatier, P. and J.-B. Senderens, *Nouvelles syntheses du methane.* Compt. Rend, 1902. **134**: p. 514-516.
11. Goodman, D.J., *Methanation of carbon dioxide.* 2013.
12. Zhang, J., et al., *Synthesis, characterization and properties of anti-sintering nickel incorporated MCM-41 methanation catalysts.* Fuel, 2013. **109**: p. 693-701.
13. Wen, Y., et al., *Cerium oxide promoted Ni/MgO catalyst for the synthesis of multi-walled carbon nanotubes.* Chinese Journal of Catalysis, 2011. **32**(6-8): p. 1323-1328.
14. Planeix, J., et al., *Application of carbon nanotubes as supports in heterogeneous catalysis.* Journal of the American Chemical Society, 1994. **116**(17): p. 7935-7936.
15. Feng, Y., W. Yang, and W. Chu, *A study of CO2 methanation over Ni-based catalysts supported by CNTs with various textural characteristics.* International Journal of Chemical Engineering, 2015. **2015**.
16. Swapnesh, A., V.C. Srivastava, and I.D. Mall, *Comparative study on thermodynamic analysis of CO2 utilization reactions.* Chemical Engineering & Technology, 2014. **37**(10): p. 1765-1777.
17. Molino, A. and G. Braccio, *Synthetic natural gas SNG production from biomass gasification–Thermodynamics and processing aspects.* Fuel, 2015. **139**: p. 425-429.
18. Miguel, C.V., et al., *Direct CO 2 hydrogenation to methane or methanol from post-combustion exhaust streams–A thermodynamic study.* Journal of Natural Gas Science and Engineering, 2015. **22**: p. 1-8.
19. Abate, S., et al., *Catalytic Performance of γ-Al2O3–ZrO2–TiO2–CeO2 Composite Oxide Supported Ni-Based Catalysts for CO2 Methanation.* Industrial & Engineering Chemistry Research, 2016. **55**(16): p. 4451-4460.
20. Jürgensen, L., et al., *Dynamic biogas upgrading based on the Sabatier process: Thermodynamic and dynamic process simulation.* Bioresource technology, 2015. **178**: p. 323-329.
21. Müller, K., et al., *Sabatier based CO 2-methanation of flue gas emitted by conventional power plants.* Energy Procedia, 2013. **40**: p. 240-248.

22. Gould, B.D., O.A. Baturina, and K.E. Swider-Lyons, *Deactivation of Pt/VC proton exchange membrane fuel cell cathodes by SO2, H2S and COS.* Journal of Power Sources, 2009. **188**(1): p. 89-95.

23. Li, L., et al., *Regeneration of sulfur deactivated Ni-based biomass syngas cleaning catalysts.* Industrial & Engineering Chemistry Research, 2010. **49**(20): p. 10144-10148.

24. Aziz, M., et al., *CO 2 methanation over Ni-promoted mesostructured silica nanoparticles: Influence of Ni loading and water vapor on activity and response surface methodology studies.* Chemical Engineering Journal, 2015. **260**: p. 757-764.

25. Tatsumi, T., et al., *Mechanical stability of mesoporous materials, MCM-48 and MCM-41.* Journal of Porous Materials, 1999. **6**(1): p. 13-17.

26. Bartholomew, C., R. Pannell, and R. Fowler, *Sintering of alumina-supported nickel and nickel bimetallic methanation catalysts in H2H2O atmospheres.* Journal of Catalysis, 1983. **79**(1): p. 34-46.

27. Mabena, L.F., et al., *Nitrogen-doped carbon nanotubes as a metal catalyst support.* Applied Nanoscience, 2011. **1**(2): p. 67-77.

28. Varshney, K., *Carbon nanotubes: a review on synthesis, properties and applications.* International Journal of Engineering Research, 2014. **2**(4): p. 660-677.

29. Odom, T.W., et al., *Atomic structure and electronic properties of single-walled carbon nanotubes.* Nature, 1998. **391**(6662): p. 62-64.

30. Ganesh, E., *Single walled and multi walled carbon nanotube structure, synthesis and applications.* International Journal of Innovative Technology and Exploring Engineering, 2013. **2**(4): p. 311-320.

31. De, M., *Catalyst Science and Technology-Web course.* 2014.

32. Panchakarla, L., A. Govindaraj, and C. Rao, *Boron-and nitrogen-doped carbon nanotubes and graphene.* Inorganica Chimica Acta, 2010. **363**(15): p. 4163-4174.

33. Saha, M.S. and A. Kundu, *Functionalizing carbon nanotubes for proton exchange membrane fuel cells electrode.* Journal of Power Sources, 2010. **195**(19): p. 6255-6261.

34. Cruz-Silva, E., et al., *Heterodoped nanotubes: theory, synthesis, and characterization of phosphorus– nitrogen doped multiwalled carbon nanotubes.* ACS nano, 2008. **2**(3): p. 441-448.

35. Iijima, S., *Helical microtubules of graphitic carbon.* nature, 1991. **354**(6348): p. 56.

36. Villalpando-Paez, F., et al., *Synthesis and characterization of long strands of nitrogen-doped single-walled carbon nanotubes.* Chemical Physics Letters, 2006. **424**(4): p. 345-352.

37. Ghosh, K., et al., *Tailoring the field emission property of nitrogen-doped carbon nanotubes by controlling the graphitic/pyridinic substitution.* Carbon, 2010. **48**(1): p. 191-200.

38. Ajayan, P., *Nanotubes from carbon.* Chemical reviews, 1999. **99**(7): p. 1787-1800.

39. Matter, P.H., E. Wang, and U.S. Ozkan, *Preparation of nanostructured nitrogen-containing carbon catalysts for the oxygen reduction reaction from SiO 2-and MgO-supported metal particles.* Journal of Catalysis, 2006. **243**(2): p. 395-403.

40. Chizari, K., et al., *Tuning of nitrogen-doped carbon nanotubes as catalyst support for liquid-phase reaction.* Applied Catalysis A: General, 2010. **380**(1): p. 72-80.

41. Amadou, J., et al., *N-doped carbon nanotubes for liquid-phase C C bond hydrogenation.* Catalysis Today, 2008. **138**(1): p. 62-68.

42. Khazaee, M., et al., *Dispersibility of vapor phase oxygen and nitrogen functionalized multi-walled carbon nanotubes in various organic solvents.* Scientific reports, 2016. **6**.

43. Hwang, S., et al., *Methane production from carbon monoxide and hydrogen over nickel–alumina xerogel catalyst: Effect of nickel content.* Journal of Industrial and Engineering Chemistry, 2011. **17**(1): p. 154-157.

44. Chang, F.-W., et al., *Hydrogenation of CO 2 over nickel catalysts on rice husk ash-alumina prepared by incipient wetness impregnation.* Applied Catalysis A: General, 2003. **247**(2): p. 309-320.

45. Falconer, J.L. and A.E. Zağli, *Adsorption and methanation of carbon dioxide on a nickel/silica catalyst.* Journal of Catalysis, 1980. **62**(2): p. 280-285.

46.   Weatherbee, G.D. and C.H. Bartholomew, *Hydrogenation of CO2 on group VIII metals: II. Kinetics and mechanism of CO2 hydrogenation on nickel.* Journal of Catalysis, 1982. **77**(2): p. 460-472.

47.   Peebles, D., D. Goodman, and J. White, *Methanation of carbon dioxide on Ni (100) and the effects of surface modifiers.* J. Phys. Chem, 1983. **87**: p. 4378-4387.

48.   Marwood, M., R. Doepper, and A. Renken, *In-situ surface and gas phase analysis for kinetic studies under transient conditions The catalytic hydrogenation of CO2.* Applied Catalysis A: General, 1997. **151**(1): p. 223-246.

49.   Lapidus, A., et al., *The mechanism of carbon dioxide hydrogenation on copper and nickel catalysts.* Petroleum Chemistry, 2007. **47**(2): p. 75-82.

50.   Fujita, S., et al., *Methanation of carbon monoxide and carbon dioxide over nickel catalyst under the transient state.* Reaction Kinetics and Catalysis Letters, 1987. **33**(1): p. 179-184.

51.   Schild, C., A. Wokaun, and A. Baiker, *On the mechanism of CO and CO2 hydrogenation reactions on zirconia-supported catalysts: a diffuse reflectance FTIR study: Part II. Surface species on copper/zirconia catalysts: implications for methanoi synthesis selectivity.* Journal of molecular catalysis, 1990. **63**(2): p. 243-254.

52.   Wagner, C., *Adsorbed atomic species as intermediates in heterogeneous catalysis.* Advances in Catalysis, 1970. **21**: p. 323-381.

53.   Panagiotopoulou, P., D.I. Kondarides, and X.E. Verykios, *Mechanistic aspects of the selective methanation of CO over Ru/TiO 2 catalyst.* Catalysis today, 2012. **181**(1): p. 138-147.

54.   Vesselli, E., et al., *Carbon dioxide hydrogenation on Ni (110).* Jung, 2008. **383**: p. 285.

55.   Sharma, S., et al., *CO 2 methanation on Ru-doped ceria.* Journal of Catalysis, 2011. **278**(2): p. 297-309.

56.   Park, H.-a., et al., *Highly porous gallium oxide with a high CO2 affinity for the photocatalytic conversion of carbon dioxide into methane.* Journal of Materials Chemistry, 2012. **22**(12): p. 5304-5307.

57.   Chew, L.M., et al., *Effect of nitrogen doping on the reducibility, activity and selectivity of carbon nanotube-supported iron catalysts applied in CO 2 hydrogenation.* Applied Catalysis A: General, 2014. **482**: p. 163-170.

58.   Lehman, J.H., et al., *Evaluating the characteristics of multiwall carbon nanotubes.* Carbon, 2011. **49**(8): p. 2581-2602.

59.   Guo, K., M. Gu, and Z. Yu, *Carbon nanocatalysts for aquathermolysis of heavy crude oil: Insights into thiophene hydrodesulfurization.* Energy Technology, 2017.

60.   Costa, S., et al., *Characterization of carbon nanotubes by Raman spectroscopy.* Mater Sci-Poland, 2008. **26**(2): p. 433-441.

61.   Brunauer, S., P.H. Emmett, and E. Teller, *Adsorption of gases in multimolecular layers.* J. Am. Chem. Soc, 1938. **60**(2): p. 309-319.

62.   Trunschke, A., *Surface Area and Pore Size Determination; Modern Methods in Heterogeneous Catalysis Research.* 2007.

63.   Instruments, Q. *Micropore Size Calculation*. 2004-2006; Available from: http://slideplayer.com/slide/3383155/.

64.   Cullity, B.D., *Answers to Problems: Elements of X-ray Diffraction*. 1978: Addison-Wesley Publishing Company.

65.   Ma, Z. and F. Zaera, *Characterization of heterogeneous catalysts.* Surface and Nanomolecular Catalysis, 2006: p. 1-37.

66.   https://vscht.cz/kat/download/lab_tpr_eng.pdf, 2017.

67.   Llauradó, M. 2007.

68.   Webb, P.A., *Introduction to chemical adsorption analytical techniques and their applications to catalysis.* Micromeritics Instrument Corp. Technical Publications, 2003.

69.   Webb, P.A. and C. Orr, *Analytical methods in fine particle technology*. 1997: Micromeritics Instrument Corp.

70.   Tada, S., et al., *N2O pulse titration of Ni/α-Al2O3 catalysts: a new technique applicable to nickel surface-area determination of nickel-based catalysts.* The Journal of Physical Chemistry C, 2013. **117**(28): p. 14652-14658.

71.   Wang, W., et al., *Mesoporous nickel catalyst supported on multi-walled carbon nanotubes for carbon dioxide methanation.* International Journal of Hydrogen Energy, 2016. **41**(2): p. 967-975.

72.   Eswaramoorthy, M., R. Sen, and C. Rao, *A study of micropores in single-walled carbon nanotubes by the adsorption of gases and vapors.* Chemical physics letters, 1999. **304**(3): p. 207-210.

73.   Li, Y.-H., et al., *Adsorption of cadmium (II) from aqueous solution by surface oxidized carbon nanotubes.* Carbon, 2003. **41**(5): p. 1057-1062.

74.   Chen, M., et al., *Effect of purification treatment on adsorption characteristics of carbon nanotubes.* Diamond and related materials, 2007. **16**(4): p. 1110-1115.

75.   Birch, M.E., et al., *Properties that influence the specific surface areas of carbon nanotubes and nanofibers.* Annals of occupational hygiene, 2013. **57**(9): p. 1148-1166.

76.   Stangeland, K., et al., *The Effect of Temperature and Initial Methane Concentration on Carbon Dioxide Methanation on Ni Based Catalysts.* Energy Procedia, 2017. **105**: p. 2016-2021.